

A Comparison of Two Shallow Water Models with Non-Conforming Adaptive Grids

Amik St-Cyr*, Christiane Jablonowski†, John M. Dennis‡

Henry M. Tufo§ and Stephen J. Thomas¶

Computational Mathematics group (CompMath),

Institute for Mathematics Applied to Geosciences (IMAGE),

National Center for Atmospheric Research||

Boulder, Colorado

Submitted to Mon. Wea. Rev. on 11/28/2006

Accepted on 8/3/2007

*Corresponding author address: National Center for Atmospheric Research (NCAR), 1850 Table Mesa Drive Boulder, CO 80305, USA, E-mail: amik@ucar.edu

†Current affiliation: University of Michigan, Department of Atmospheric, Oceanic and Space Sciences, 2455 Hayward St., Ann Arbor, MI 48109, USA

‡National Center for Atmospheric Research (NCAR), 1850 Table Mesa Drive Boulder, CO 80305, USA

§Second affiliation: University of Colorado Boulder, 430 UCB Boulder, CO 80309-0430, USA

¶National Center for Atmospheric Research (NCAR), 1850 Table Mesa Drive Boulder, CO 80305, USA

||The National Center for Atmospheric Research is sponsored by the National Science Foundation.

Abstract

In an effort to study the applicability of adaptive mesh refinement (AMR) techniques to atmospheric models an interpolation-based spectral element shallow water model on a cubed-sphere grid is compared to a block-structured finite volume method in latitude-longitude geometry. Both models utilize a non-conforming adaptation approach which doubles the resolution at fine-coarse mesh interfaces. The underlying AMR libraries are quad-tree based and ensure that neighboring regions can only differ by one refinement level.

The models are compared via selected test cases from a standard test suite for the shallow water equations, and via a barotropic instability test. These tests comprise the passive advection of a cosine bell and slotted cylinder, a steady-state geostrophic flow, a flow over an idealized mountain, a Rossby-Haurwitz wave and the evolution of a growing barotropic wave. Both static and dynamics adaptations are evaluated which reveal the strengths and weaknesses of the AMR techniques. Overall, the AMR simulations show that both models successfully place static and dynamic adaptations in local regions without requiring a fine grid in the global domain. The adaptive grids reliably track features of interests without visible distortions or noise at mesh interfaces. Simple threshold adaptation criteria for the geopotential height and the relative vorticity are assessed.

1. Introduction

Simulating the climate is a grand challenge problem requiring multiple, century-long integrations of the equations modeling the Earth's atmosphere. Consequently, grid resolutions in atmospheric climate models are much coarser than in numerical weather prediction models, where accurate predictions are limited to about ten days. However, it has been recognized that localized flow structures, like hurricanes, may play an important role in obtaining the correct climate signal. In particular, there exists a requirement for localized mesh refinement in regional climate modeling studies. It is also conjectured, at this time, that the lack of resolution in the tropics is the cause of the inability of most climate models to capture the statistical contribution of extreme weather events.

While mesh adaptation is a mature field in computational fluid dynamics, currently, the only fully operational adaptive weather and dispersion model is OMEGA (Bacon et al. 2000; Gopalakrishnan et al. 2002). The latter is based on the finite-volume approach and uses conforming Delaunay meshes that are locally modified and smoothed. Researchers involved in hurricane or typhoon predictions were amongst the very first to experiment with variable resolutions in atmospheric models. The preferred method consisted of nesting finer meshes statically into coarser ones (Kurihara et al. 1979; Kurihara and Bender 1980). Nesting is a wide spread technique in current models, especially mesoscale models, to achieve high resolutions (Frohn et al. 2002) in local regions. Truly adaptive models were first developed by Skamarock et al. (1989), Skamarock and Klemp (1993) and Dietachmayer and Droegemeier (1992). Skamarock and Klemp (1993) based their adaptive mesh refinement (AMR) strategy on a truncation error estimate (Skamarock 1989). Continuing in the realm of second order conforming methods Iselin et al. (2002) developed a dynamically adaptive Multidimensional Positive Definite Advection Transport Algorithm (MPDATA) (Iselin et al. 2005). MPDATA was thoroughly reviewed in Smolarkiewicz (2006) because of its various numerical qualities. The discussion addressed generalized space-time coordinates that enable continuous mesh deformations (Prusa and Smolarkiewicz 2003) as well as the generalization of MPDATA to

unstructured grids (Smolarkiewicz and Szmelter 2005). Recently, Fox-Rabinovitz et al. (2006) also discussed results of various climate models with stretched grids that statically refined prescribed regions of interest. Dynamically adaptive schemes on the sphere were discussed by Jablonowski (2004), Läuter (2004), Behrens et al. (2005) and Läuter et al. (2007) where only Jablonowski et al. (2004) utilizes a non-conforming approach. Both AMR models considered in this work are of the non-conforming type. The latter corresponds to meshes where elements, or control volumes, might share more than one neighboring element per face. Meshes where exactly two elements share a face are called conforming. A review of adaptive methods in atmospheric modeling is given in Behrens (2006).

It is recognized that high-order spatial resolution is necessary in climate modeling. To paraphrase Boyd (2004), spectral methods like Continuous Galerkin (CG) or Discontinuous Galerkin (DG) are blessedly free of the spurious wave dispersion induced by low-order methods¹. The corresponding reduction in grid points directly lowers the amount of costly column physics evaluations. Multiple efforts to include conforming mesh refinement techniques in models with high-order numerical methods were initiated Giraldo (2000), Fournier et al. (2004), Giraldo and Warburton (2005), Giraldo (2006) and Rosenberg et al. (2006). However, supporting conforming adaptive meshes strongly restricts the time steps that obey the Courant-Friedrich-Levy (CFL) stability condition. One solution is to consider non-conforming elements or blocks, ideally with sub-cycled time steps in refined regimes.

In this paper two adaptive mesh techniques for 2D shallow water flows on the sphere are compared. In particular, the study focuses on the characteristics of the AMR approach in the cubed-sphere spectral element model (SEM) by St-Cyr (2006) and compares it to the adaptive finite volume (FV) method by Jablonowski et al. (2006). Both SEM and FV are AMR models of the non-conforming type. A thorough study of the dynamically adaptive FV scheme based on quadrilateral control volumes can also be found in Jablonowski (2004). In particular, 2D shallow water and 3D primitive-equation numerical experiments were conducted using a latitude-longitude grid on the

¹The quote actually starts with: "It is all about the waves stupid: ..."

sphere. This adaptive model is built upon the finite volume technique by Lin and Rood (1996) and Lin and Rood (1997). The spectral element model is based on the ideas of Patera (1984). The non-conforming treatment follows the interpolation procedure by Fischer et al. (2002). The spectral element method was originally developed for incompressible fluid flows. Meanwhile, it has been adapted by many authors (Haidvogel et al. 1997; Taylor et al. 1997; Giraldo 2001; Thomas and Loft 2002) for global atmospheric and oceanic simulations.

The paper is organized as follows. In Section 2 the shallow water equations are introduced which are the underlying equation for our model comparison. Both models SEM and FV are briefly reviewed in Section 3. This includes a discussion of the adaptive mesh approach for the spectral elements in SEM and the latitude-longitude blocks in FV. In Section 4 the characteristics of the AMR techniques are tested using selected test cases from the Williamson et al. (1992) shallow water test suite and the Galewsky et al. (2004) test. They comprise the advection of a cosine bell and slotted cylinder, a steady-state geostrophic flow, a flow over a mountain, a Rossby-Haurwitz wave and the evolution of a barotropic wave. This section also addresses selected computational aspects of the AMR approaches. The findings are summarized in Section 5.

2. Shallow water equations

The shallow water equations have been used as a test bed for promising numerical methods by the atmospheric modeling community for many years. They contain the essential wave propagation mechanisms found in atmospheric General Circulation Models (GCMs). The linearized primitive equations yield a series of layered shallow water problems where the mean depth of each layer is related to the maximum wave speed supported by the medium. These are the fast-moving gravity waves and nonlinear Rossby waves. The latter are important for correctly capturing nonlinear atmospheric dynamics. The governing equations of motion for the inviscid flow of a free surface

are given by

$$\frac{\partial \mathbf{v}}{\partial t} + (f + \zeta) \mathbf{k} \times \mathbf{v} + \frac{1}{2} \nabla (\mathbf{v} \cdot \mathbf{v}) + \nabla (\Phi + \Phi_s) = 0 \quad (1)$$

$$\frac{\partial \Phi}{\partial t} + \nabla \cdot (\Phi \mathbf{v}) = 0 \quad (2)$$

where t is the time, $\Phi = gh$ symbolizes the geopotential, h is the depth of the fluid and g denotes the gravitational acceleration. Furthermore, $\Phi_s = gh_s$ is the surface geopotential, h_s symbolizes the height of the orography, $\mathbf{v} = (u, v)^T$ stands for the horizontal velocity vector with the zonal and meridional wind components u and v , \mathbf{k} denotes the radial outward unit vector, and f and ζ are the Coriolis parameter and relative vorticity, respectively. ∇ indicates the horizontal gradient operator, whereas $\nabla \cdot$ stands for the horizontal divergence operator. The momentum equation (1) is written in its vector-invariant form.

Note that in the FV model, a divergence damping term is added to Eq. (1) which reduces gravitational noise that is associated with high-frequency variations of the divergence field. This leads to the modified momentum equation

$$\frac{\partial \mathbf{v}}{\partial t} + (f + \zeta) \mathbf{k} \times \mathbf{v} + \frac{1}{2} \nabla (\mathbf{v} \cdot \mathbf{v}) + \nabla (\Phi + \Phi_s - cD) = 0 \quad (3)$$

where c is the coefficient of the divergence damping and D stands for the divergence. In spherical coordinates D is given by

$$D = \frac{1}{a \cos \phi} \left[\frac{\partial u}{\partial \lambda} + \frac{\partial}{\partial \phi} (v \cos \phi) \right] \quad (4)$$

Here, a symbolizes the radius of the Earth, and λ and ϕ denote the longitudinal and latitudinal directions, respectively. The details about the choice of the resolution-, position- and time step dependent coefficient c are documented in Jablonowski (2004).

3. Description of the adaptive shallow water models

The spectral element method (SEM) is a combination of ideas coming from the finite-element method and of the spectral method. The order of accuracy is determined by the degree of the local basis functions within a finite element. The basis consists of Lagrange polynomials passing through Gauss-Legendre-Lobatto (GLL) or Gauss-Legendre (GL) quadrature points facilitating greatly the evaluation of the integrals appearing in a weak formulation. For the tests here, fifth degree basis functions for scalars are employed which utilize 6×6 GL quadrature points per spectral element. The SEM grid is based on a projection of a cube inscribed into a sphere (Sadourny (1972)), a so-called cubed-sphere grid which consists of 6 faces. These are further subdivided into spectral elements quadrangles which are evenly distributed over the surface of the sphere in the non-adapted case. Note that the numerical approach in SEM is non-monotonic and does not conserve mass. Nevertheless, the variation in the total mass is small over typical forecast periods of two weeks.

This is in contrast to the monotonic and mass-conservative FV model which was originally developed by Lin and Rood (1997). It utilizes the third order Piecewise Parabolic Method (PPM) (Colella and Woodward 1984) which was first designed for compressible fluids with strong shocks. The PPM algorithm applies monotonicity constraints that act as a nonlinear scale-selective dissipation mechanism. This dissipation primarily targets the flow features at the smallest scales.

Both shallow water models are characterized in more detail below. In particular, the individual adaptive mesh approaches are described which implement adaptations in the horizontal directions. The time step, on the other hand, is not adapted, except for selected advection tests. Therefore, the chosen time step must be numerically stable on the finest grid in an adapted model run.

a. Spectral element (SEM) shallow water model

1. CURVILINEAR COORDINATES: CUBED SPHERE

The flux form shallow-water equations in curvilinear coordinates are described in Sadourny (1972).

Let \mathbf{a}_1 and \mathbf{a}_2 be the covariant base vectors of the transformation between inscribed cube and spherical surface. The metric tensor of the transformation is defined as $G_{ij} \equiv \mathbf{a}_i \cdot \mathbf{a}_j$. Covariant and contravariant vectors are related through the metric tensor by $u_i = G_{ij}u^j$ and $u^i = G^{ij}u_j$, where $G^{ij} = (G_{ij})^{-1}$ and $G = \det(G_{ij})$. The six local coordinate systems (x^1, x^2) are based on an equiangular central projection, $-\pi/4 \leq x^1, x^2 \leq \pi/4$. The metric tensor for all six faces of the cube is

$$G_{ij} = \frac{1}{r^4 \cos^2 x^1 \cos^2 x^2} \begin{bmatrix} 1 + \tan^2 x^1 & -\tan x^1 \tan x^2 \\ -\tan x^1 \tan x^2 & 1 + \tan^2 x^2 \end{bmatrix} \quad (5)$$

where $r = (1 + \tan^2 x^1 + \tan^2 x^2)^{1/2}$ and $\sqrt{G} = 1/r^3 \cos^2 x^1 \cos^2 x^2$.

The shallow water equations are written in curvilinear coordinates using the following definitions for divergence and vorticity

$$\nabla \cdot \mathbf{v} \equiv \frac{1}{\sqrt{G}} \left[\frac{\partial}{\partial x^i} (\sqrt{G} u^i) \right], \quad \zeta \equiv \frac{\epsilon_{ij}}{\sqrt{G}} \frac{\partial u_j}{\partial x^i} = \frac{1}{\sqrt{G}} \left[\frac{\partial u_2}{\partial x^1} - \frac{\partial u_1}{\partial x^2} \right]$$

and replacing them in (2). In their contravariant form the equations are

$$\frac{\partial u^i}{\partial t} + G^{ij} \left[\frac{\partial}{\partial x^j} (u^k u_k) + \frac{\partial \Phi}{\partial x^j} + \sqrt{G} \epsilon_{jk} u^k (f + \zeta) \right] = 0, \quad (6)$$

$$\frac{\partial \Phi}{\partial t} + u^j \frac{\partial \Phi}{\partial x^j} + \frac{\Phi}{\sqrt{G}} \frac{\partial}{\partial x^j} (\sqrt{G} u^j) = 0 \quad (7)$$

where the Einstein summation convention is used for repeated indices and ϵ_{ij} is a permutation matrix. Additional information on the equation set can also be found in Nair et al. (2005).

2. SPATIAL AND TEMPORAL DISCRETIZATION

The equations of motion are discretized in space using the $\mathbb{P}_N - \mathbb{P}_{N-2}$ spectral element method as in Thomas and Loft (2002). The cubed-sphere is partitioned into K elements Ω^k in which the dependent and independent variables are approximated by tensor-product polynomial expansions. The velocity on element Ω^k is expanded in terms of the N -th degree Lagrangian interpolants h_i

$$\mathbf{v}_h^k(\mathbf{x}) = \sum_{i=0}^N \sum_{j=0}^N \mathbf{v}_{ij}^k h_i(\xi^k(\mathbf{x})) h_j(\eta^k(\mathbf{x})) \quad (8)$$

and the geopotential is expanded on the same element using the $(N - 2)$ -th degree interpolants \tilde{h}_i

$$\Phi_h^k(\mathbf{x}) = \sum_{i=1}^{N-1} \sum_{j=1}^{N-1} \Phi_{ij}^k \tilde{h}_i(\xi^k(\mathbf{x})) \tilde{h}_j(\eta^k(\mathbf{x})) \quad (9)$$

where $\mathbf{x} \rightarrow (\xi^k(\mathbf{x}), \eta^k(\mathbf{x}))$ is an affine transformation from the element Ω^k on the cubed sphere to the reference element $[-1, 1] \times [-1, 1]$ pictured in Fig. 1. A weak Galerkin formulation results from the integration of the equations with respect to test functions and the direct evaluation of inner products using Gauss-Legendre and Gauss-Lobatto-Legendre quadrature. The positions of the corresponding GL and GLL quadrature points within each spectral element with mapped coordinates ξ and η are depicted in Fig. 1. The GLL points for the co-located velocity components are marked by the circles, the open squares point to the GL points for scalars. The polynomial degrees are 7 and 5, respectively. An overview of the chosen parameters and base resolutions for the present study is also given in Table 1.

C^0 continuity of the velocity is enforced at inter-element boundaries sharing Gauss-Lobatto-Legendre points and Direct Stiffness Summation (DSS) is then applied (Deville et al. 2002). The advection operator in the momentum equation is expressed in terms of the relative vorticity and kinetic energy, whereas the continuity equation relies on the velocity form. Wilhelm and Kleiser (2000) have shown that the rotational form of the advection operator is stable for the $\mathbb{P}_N - \mathbb{P}_{N-2}$ spectral element discretization. A standard Asselin-Robert filtered leap-frog discretization is em-

ployed for integrating the equations of motion in time. More advanced options, that are tailored for AMR based on the ideas in St-Cyr and Thomas (2005a), are described in St-Cyr (2006). Since a spectral basis is employed in each element, the spectrum of the advective operators must be corrected using a 2/3-rule similar to what is employed in global pseudo spectral models. A Boyd-Vandeven filter (Vandeven 1991; Boyd 1996) was used during the adaptive numerical simulations that removes the last third of the spectrum.

3. NON-CONFORMING SPECTRAL ELEMENTS

The positions of the collocation points at the boundaries of non-conforming spectral elements do not coincide and a procedure is required to connect neighboring elements. Several techniques are available including mortars (Mavriplis 1989; Feng and Mavriplis 2002) and interpolations (Fischer et al. 2002). Here, interpolations are used. The true unknowns at a boundary belong to the master coarse element and are passed to the refined slave elements by the following procedure. From Eq. (8), at one of the element boundaries $\Gamma_{km} = \Omega_k \cap \Omega_m$ with $\xi^k = \xi^m = 1$, the trace of the solution is

$$\mathbf{v}(\mathbf{x}(\xi^k, \eta^k))_h^k|_{\Gamma_{km}} = \mathbf{v}_h^k(\mathbf{x}(1, \eta^k)) = \sum_{j=0}^N \mathbf{v}_{Nj}^k h_j(\eta^k) \quad (10)$$

where h_j are the Lagrange interpolants defined at the GLL points. To interpolate the master solution to the slave edge, a mapping is created from the master reference element relative to the slave's reference element. Let η_m^l denote this mapping, then

$$\eta_m^l(\eta) := \frac{\eta}{2^l} + \frac{2m-1}{2^l} - 1 \quad (11)$$

where $m \in [1, 2^l]$ is the slave face number and l is the number of the refinement level. This spatial refinement strategy is called h -refinement which is in contrast to increasing the order of the polynomials (p -refinement).

Interpolations can be expressed in matrix form as

$$[J_m^l]_{ij} = h_j(\eta_m^l(\xi_i)) \quad (12)$$

where $\{\xi_i\}_{i=0}^N$ are the Gauss-Legendre-Lobatto points used in the quadrature and in the collocation of the dependent variables. If \mathbf{v}^k are the unknowns on the edge of the master element, then $J_m^l \mathbf{v}^k$ represents the master element contributions passed to the slave elements. Assembly of the global spectral element matrix is not viable on today's computer architectures with distributed memory. Instead, the action of the assembled matrix on a vector is performed with the help of DSS. For A , a matrix resulting from the spectral element discretization of a differential operator, defined for the true degrees of freedom and A_L , the block diagonal matrix of the individual local unassembled contributions of each element as if they were disjoint, the DSS for conforming elements is represented by

$$v^T Au = v^T Q^T A_L Q u \quad (13)$$

where Q is a Boolean rectangular matrix² representing the scattering of the true degrees of freedom to the unassembled blocks (one block in A_L per element). A non-conforming formulation can be obtained by replacing the scattering Boolean matrices Q with $Q = J_L \tilde{Q}$

$$v^T Au = v^T (\tilde{Q}^T J_L^T) A_L (J_L \tilde{Q}) u. \quad (14)$$

Note that Q is not Boolean anymore but now \tilde{Q} is. The block diagonal matrix J_L consist of the identity where the interfaces between elements match and of the interpolation matrix (12) where interfaces are non-conforming. To facilitate time-stepping procedures, the matrix must be lumped by summing rows in the mass matrix (Quarteroni and Valli 1997). Let $L(A)$ represent the lumping operation. Lumping the global matrix A is equivalent to lumping the local matrix $J_L^T A_L J_L$ and it

²Matrix containing at least a 1 per line.

can be shown that

$$L(A) = L(\tilde{Q}^T J_L^T A_L J_L \tilde{Q}) = \tilde{Q}^T L(J_L^T A_L J_L) \tilde{Q}. \quad (15)$$

4. ADAPTATION PRINCIPLE

The adaptation algorithm developed here is parallel and usable on distributed memory computers. The cubed sphere is initially tiled with an uniform, low resolution mesh and each element represents the root of a quad-tree. While a quad-tree is a natural description for two dimensional mesh refinement, the six faces of the cubed-sphere geometry necessitate a graph data structure. For the quad-trees, a set of simple bit manipulation subroutines are used to provide inheritance information. A graph data structure which describes the connection between the roots and leaves of each quad-tree is also maintained. To simplify the interface management, neighboring elements are restricted to be at most one level of refinement apart. When elements are marked for refinement, a parallel procedure verifies that a compatible quad-tree refinement exists, with respect to all the roots and the interface restriction. The communication package is properly modified to enable correct inter-element communications related to the DSS procedure. This was greatly simplified by replacing the graph-based communication package in the model by the more generic one developed by Tufo (1998). If a load imbalance is detected then the partitioning algorithm is invoked and elements are migrated to rebalance the workload on each processor. Apart from the Message Passing Interface (MPI) library, the graph partitioning tool PARMETIS(Karypis et al. 2002) and the generic DSS libraries, no other specialized high-level library is used. The non-adapted spectral element model also supports an efficient space-filling curve loadbalancing approach (Dennis 2003) which we plan to use in the adaptive model for future simulations.

b. Finite volume (FV) shallow water model

1. MODEL DESCRIPTION

The adaptive finite volume model is built upon the advection algorithm by Lin and Rood (1996) and its corresponding shallow water system (Lin and Rood 1997). The FV shallow water model is comprised of the momentum equation and mass continuity equation as shown in Eqs. (1) and (2). Here the flux-form of the mass conservation law and the vector-invariant form of the momentum equation are selected. In addition, a divergence damping term is added to the momentum equation which is outlined in section 2.

The finite-volume dynamical core utilizes a flux form algorithm for the horizontal advection processes, which, from the physical point of view, can be considered a discrete representation of the conservation law in finite-volume space. However, from the mathematical standpoint, it can be viewed as a numerical method for solving the governing equations in integral form. This leads to a more natural and often more precise representation of the advection processes, especially in comparison to finite difference techniques. The transport processes, e.g. for the height $h = \Phi/g$ of the shallow water system, are modeled by fluxes into and out of the finite control-volume where volume-mean quantities are predicted

$$\begin{aligned} \bar{h}_{i,j}^{n+1} = \bar{h}_{i,j}^n &- \frac{\Delta t}{a \cos \phi_j \Delta \lambda_i} (F_{i+\frac{1}{2},j} - F_{i-\frac{1}{2},j}) \\ &- \frac{\Delta t}{a \cos \phi_j \Delta \phi_j} (\cos \phi_{j+\frac{1}{2}} G_{i,j+\frac{1}{2}} - \cos \phi_{j-\frac{1}{2}} G_{i,j-\frac{1}{2}}). \end{aligned} \quad (16)$$

Here, the overbar $\bar{(\)}$ indicates the volume-mean, F and G denote the time-averaged 1D numerical fluxes in longitudinal and latitudinal direction which are computed with the upstream-biased and monotonic PPM scheme (see also Carpenter et al. (1990) and Nair and Machenhauer (2002)). Δt symbolizes the time step, a stands for the radius of the Earth, the indices i and j point to grid point locations in the longitudinal (λ) and latitudinal (ϕ) direction and the index n marks the discrete time level. In addition, $\Delta \lambda_i = (\lambda_{i+\frac{1}{2}} - \lambda_{i-\frac{1}{2}})$ and $\Delta \phi_j = (\phi_{j+\frac{1}{2}} - \phi_{j-\frac{1}{2}})$ represent the longitudinal and latitudinal grid distances measured in radians.

The advection algorithm shown in Eq. (16) is the fundamental building block of the horizontal discretization in the FV shallow water model. It is not only used to predict the time evolution of the mass (Eq. (2)), but also determines the absolute vorticity fluxes and kinetic energy in the momentum equation. Further algorithmic details of the shallow water code are described in Lin and Rood (1997) who also discussed the staggered Arakawa C and D grid approach utilized in the model.

2. BLOCK-STRUCTURED ADAPTIVE MESH APPROACH

The AMR design of the FV shallow water model is built upon a 2D block-structured data configuration in spherical coordinates. The concept of the block data structure and corresponding resolutions is fully described in Jablonowski et al. (2006). In essence, a regular latitude-longitude grid is split into $B_y \times B_x$ non-overlapping spherical blocks that span the entire sphere. Each block is logically rectangular and comprises a constant number of $N_y \times N_x$ grid points in latitudinal and longitudinal direction. If, for example, 6×9 grid points per block are selected with $B_y \times B_x = 6 \times 8$ blocks on the sphere then the configuration corresponds to a $5^\circ \times 5^\circ$ uniform mesh resolution. Here, we use such an initial configuration for selected test cases in Section 4. All blocks are self-similar and split into four in the event of refinement requests, thereby doubling the spatial resolution. Coarsenings reverse this refinement principle. Then four “children” are coalesced into a single self-similar parent block which reduces the grid resolution in each direction by a factor of 2. As in SEM neighboring blocks can only differ by one refinement level. This leads to cascading refinement areas around the finest mesh region. In addition, the blocks adjacent to the poles are kept at the same refinement level due to the application of a polar fast Fourier transform (FFT) filter in longitudinal direction. The filter stabilizes the fast waves that originate from the pressure gradient terms. Therefore, the filter is applied in tests of the full shallow water equations, but is neither needed nor applied in pure advection examples.

The FV model supports static and dynamic adaptations which are managed by an adaptive block-structured grid library for parallel processors (Oehmke and Stout 2001; Oehmke 2004).

This library utilizes a quad-tree representation of the adapted grid which is similar to the adaptive mesh technique in SEM. The communication on parallel computer architectures is performed via MPI. Our load-balancing strategy aims at assigning an equal workload to each processor which is equivalent to an equal number of blocks in the FV shallow water model. No attempt is made to keep geographical regions on the same processor. This can be achieved by a space-filling curve load-balancing strategy as in Dennis (2003) which reduces the communication overhead. Such an approach is the subject of future research. The refinement criteria are user selected. In particular, simple geopotential height thresholds or vorticity-based criteria are assessed for our dynamic adaptation tests. For static adaptations though, we place the fine-grid nests in pre-determined regions like mountainous areas or geographical patches of interest.

Each block is surrounded by ghost cell regions that share the information along adjacent block interfaces. This makes each block independent of its neighbors since the solution technique can now be individually applied to each block. The ghost cell information ensures that the requirements for the numerical stencils are satisfied. The algorithm then loops over all available blocks on the sphere before a communication step with ghost cell exchanges becomes necessary. The number of required ghost cells highly depends on the numerical scheme. Here, three ghost cells in all horizontal directions are needed which are kept at the same resolution as the inner domain of the block. The consequent interpolation and averaging techniques are further described in Jablonowski (2004) and Jablonowski et al. (2006).

The time-stepping scheme is explicit and stable for zonal and meridional Courant numbers $|\text{CFL}| < 1$. This restriction arises since the semi-Lagrangian extension of the Lin and Rood (1996) advection algorithm is not utilized in the AMR model experiments. This keeps the width of the ghost cell regions small, but on the other hand requires small time steps if high wind speeds are present in polar regions. Then the CFL condition is most restrictive due to the convergence of the meridians in the latitude-longitude grid. Therefore, we restrict the adaptations near the pole to fewer refinement levels.

The adaptive grids of both models are compared in Fig. 2. Here, an idealized mountain as

indicated by the contour lines is refined at the maximum refinement level of 3. This corresponds to the grid resolution $0.625^\circ \times 0.625^\circ$ in the finest adaptation region. The adaptive elements (SEM) and blocks (FV) overlay the sphere. The differences between the two adaptive meshes are clearly visible. The SEM model (Fig. 2a) utilizes a non-orthogonal cubed-sphere geometry and places the refined spectral elements across an edge of two cubed-sphere faces. The FV model (Fig. 2b) is formulated on a latitude-longitude grid. This leads to orthogonal blocks which are closely spaced in polar regions.

4. Numerical experiments

For our AMR model intercomparison, we select test cases with increasing complexity from the standard Williamson et al. (1992) shallow water test suite. This test suite assesses scenarios that are mainly characterized by large-scale and rather smooth flows. Therefore, we also simulate the advection of a slotted cylinder and the evolution of a barotropic wave (Galewsky et al. 2004) that both exhibit sharp gradients. The latter is an example of a strongly nonlinear test that challenges the models' dissipation and filtering mechanisms. Our discussion of the adaptive models is focused on the passive advection of a cosine bell (test case 1) and slotted cylinder with various rotation angles, a steady-state geostrophic flow (test case 2), a flow over an idealized mountain (test case 5), a Rossby-Haurwitz wave with wavenumber 4 (test case 6) and a growing barotropic wave. Both static and dynamic refinement areas are addressed that highlight the strengths and weaknesses of the two AMR approaches.

Some basic statistics of the adaptive simulations can be found in Table 2. The table lists not only the test case numbers or abbreviations with corresponding rotation angles α and base resolutions, but also gives information on the AMR approach, the number of refinement levels, the time steps as well as the number of adapted elements (SEM) and blocks (FV) at certain snapshots in time. These snapshots do not necessarily reflect the absolute maximum of adapted elements or blocks during the course of the integrations. Note that the time steps are not optimized for per-

formance. Rather they are selected to guarantee that the CFL numbers are less than unity. This guarantees numerical stability in the chosen algorithms. The CFL number is computed using the maximum possible velocity and the smallest refined cell. Note that the CFL restriction is more stringent for SEM than for FV. This is due to the clustering of GLL quadrature points (see Figure 1). The latter imposes a $O(\frac{h}{N^2})$ asymptotic behavior on the time-step size of the spectral element core with N being the polynomial degree and h the element width. The model results are typically evaluated via normalized l_1 , l_2 and l_∞ error norms. The definitions of the norms are given in Williamson et al. (1992). For the adaptive FV shallow water model the computation of the norms is also explained in Jablonowski et al. (2006).

a. Passive advection of a cosine bell

We start our intercomparison of the two AMR approaches with the traditional solid body rotation of a cosine bell around the sphere (see test case 1 in Williamson et al. (1992) for the initial conditions). This test evaluates the advective component of the numerical method in isolation. It challenges the spectral element method of SEM due to possible over- and undershoots of the transported feature. They are due to the so-called Gibbs phenomenon which is characteristic for spectral approaches (Gibbs 1899; Vandeveen 1991; Boyd 1996). Several values for the rotation angle α can be specified. It determines the angle between the axis of the solid body rotation and the poles in the spherical coordinate system. Here, we mainly report results for $\alpha = 45^\circ$ which advects the cosine bell slantwise over four corner points and two edges of the cubed-sphere. In addition, results for $\alpha = 0^\circ$ (transport along the equator) and $\alpha = 90^\circ$ (transport over the poles) are discussed. The length of the integration is 12 days which corresponds to one complete revolution of the cosine bell around the sphere. The base resolution for both shallow water models is a $5^\circ \times 5^\circ$ coarse mesh with additional initial refinements surrounding the cosine bell. In particular, the base resolution in SEM is represented by 54 elements (see Table 1) whereas the adaptations in FV start from 6×8 initial blocks. We test the refinement levels 1, 2, 3 and 4 which are equivalent to the resolutions $2.5^\circ \times 2.5^\circ$, $1.25^\circ \times 1.25^\circ$, $0.625^\circ \times 0.625^\circ$ and $0.3125^\circ \times 0.3125^\circ$ within the refined areas. Note

that these grid spacings only represent approximate resolutions for SEM because of the clustering of the collocation points near the element boundaries (see Fig. 1).

In both models we refine the grid if the geopotential height field of the cosine bell exceeds $h \geq 53$ m. This value corresponds to approximately 5% of the initial peak value with $h_{max} = 1000$ m. Of course, other refinement thresholds are also feasible. The threshold has been chosen since the refined area now tightly surrounds the cosine bell in the regular latitude-longitude grid (model FV). In SEM though, the adaptations are padded by a one-element wide halo. This leads to a broader refined area in comparison to FV and therefore, fewer invocations of the grid adaptation algorithm. For the FV model, the adaptation criterion is evaluated at every time step, whereas the criterion is checked every 20 minutes in SEM. The time steps in the FV simulations are variable and match a CFL stability criterion of $|CFL| \leq 0.95$ at the finest refinement level. This setup corresponds exactly to the adaptive advection experiments with FV in Jablonowski et al. (2006). For the SEM model, the time step is constant and restricted by the CFL number computed on the finest grid. The grid is refined up to the maximum refinement level whenever the refinement criterion is met by at least grid point within a block (FV) or spectral element (SEM). Grid coarsenings are invoked after the cosine bell left the refined area and consequently, the criterion in the whole block or spectral element is no longer fulfilled.

Figure 3 shows snapshots of the cosine bell with rotation angle $\alpha = 45^\circ$ and three refinement levels ($0.625^\circ \times 0.625^\circ$) at day 3, 6, 9 and 12. The SEM model with its refined spectral elements on the cubed sphere is depicted in the left column (Fig. 3a-d), the right column (Fig. 3e-g) displays the FV model with its block-structured latitude-longitude grid. Note that each spectral element (SEM) contains additional 6×6 GL grid points, whereas each block (FV) consists of 6×9 grid points in the latitudinal and longitudinal direction, respectively. In both models the initial state (not shown) resembles the final state (day 12) very closely. It can clearly be seen that the adapted grids of both models reliably track the the cosine bell without visible distortion or noise.

The errors can be further assessed in Fig. 4 which shows the time traces of the normalized l_1 , l_2 and l_∞ norms of the geopotential height field for rotation angle $\alpha = 45^\circ$. At this rotation

angle the errors in SEM are an order of magnitude smaller than the errors in FV. The errors in FV reach their maximum at $\alpha = 45^\circ$. This is mainly due to the use of the latitude-longitude grid and the very nature of upwind-biased finite-volume schemes. Note, that the FV algorithm is fully multi-dimensional and does not exhibit operator-splitting errors. The errors in FV are lower at other rotation angles with minimum errors at rotation angle $\alpha = 0^\circ$ which describes a pure one-dimensional transport in longitudinal direction. The sensitivity to the angle in the FV transport algorithm is closely connected to the choice of the latitude-longitude grid. On other computational grids, like a cubed-sphere or icosahedral mesh, the FV algorithm is expected to show a much weaker sensitivity (S.-J. Lin and J.-L. Lee, personal communication). The errors in SEM on the cubed-sphere mesh are independent of α . It is also apparent that SEM transports the cosine bell rather smoothly across the corners of the cubed mesh.

The error norms for $\alpha = 0^\circ$ are shown in Table 3 that documents the normalized height errors as well as the absolute maximum and minimum of the height field after one full revolution for the refinement levels 1 through 4. The errors of both models at any refinement level are now comparable to each other. In addition, the table shows that SEM introduces undershoots during the simulation which are documented by the negative minimum height values h_{min} . This is not the case for the monotonic and conservative FV advection algorithm. Here it can also be seen that the maximum height of the cosine bell h_{max} in FV is affected by the monotonicity constraint which acts as a nonlinear dissipation mechanism. It consequently reduces the peak amplitude of the cosine bell, especially at lower resolutions when the bell is not well-resolved. This decrease in maximum amplitude is less profound in SEM.

Another snapshot of the cosine bell advection test at day 3 with three refinement levels is shown in Fig. 5. Here, the rotation angle is set to $\alpha = 90^\circ$ which directs the bell straight over the poles. At day 3, the bell reaches the North Pole and both models refine the grid reliably over this region. Nevertheless, a distinct difference between the two models is the total number of refined elements (SEM) and blocks (FV) needed at high latitudes. While SEM (Fig. 5a) keeps the total number of adapted elements small in the chosen cubed-sphere geometry, the FV model (Fig. 5b) needs to

refine a large number of blocks due to the convergence of the meridians in the latitude-longitude mesh. This leads to an increase in the computational workload in the adaptive FV experiment due to the increased number of blocks and small time steps needed in polar regions. In this FV run the time step varies between approximately $\Delta t = 600$ s and $\Delta t = 10$ s which strongly depends on the position of the cosine bell (Jablonowski et al. 2006). The SEM model though utilizes a constant time step of $\Delta t = 10$ s. Further statistics for test case 1 are listed in Table 2. In particular, for rotation angle $\alpha = 45^\circ$ the number of refined blocks in FV is smaller than the number of refined elements in SEM. This effect is mainly due to the additional halo region in SEM.

Table 4 shows selected run time statistics for the adapted and uniform cosine bell advection simulations. In particular, the adaptive SEM and FV runs with three refinement levels are compared to the corresponding uniform $0.625^\circ \times 0.625^\circ$ resolution runs with $\alpha = 45^\circ$ and $\alpha = 0^\circ$ (FV only). The table lists not only the l_2 and l_∞ height error norms at day 12 but also gives information on the maximum number of refined elements and blocks, the number of time steps to complete a full revolution, the time step lengths and the wall clock times for a 12-day simulation on a single 1.9GHz IBM POWER5+ processor. Note that the FV time steps indicated by ' \approx ' are adaptive to match a CFL number of 0.95. The table therefore lists the most dominant FV time steps during the model run. Both models were compiled with identical compiler options. Note that the two models represent an initial functional implementations, whose primary concern was correctness not performance. The table shows that the AMR simulations run considerably faster than the corresponding uniform-mesh simulations despite the additional overhead that the AMR approach invokes. This is in particular true if an adaptive time step is utilized as demonstrated by the FV $\alpha = 45^\circ$ model run. In this simulation, the speedup factor is approximately 123. If identical time steps are used as in the FV $\alpha = 0^\circ$ and SEM $\alpha = 45^\circ$ examples, the speedup factors lie between 6 and 12. Then the speedup is exclusively due to the reduced work load in the adaptive simulations. Overall, the run times of the uniform FV and SEM simulations with rotation angle $\alpha = 45^\circ$ are comparable. At the rotation angle $\alpha = 0^\circ$ though, the FV model completes the 12-day simulations after a very short time period (76 s in the uniform case, 12 s in the adapted case) whereas the SEM

$\alpha = 0^\circ$ simulation with $\Delta t = 10$ s (not shown) requires a similar wall clock time as the SEM $\alpha = 45^\circ$ run. This effect is mainly due to the increased time step length in FV ($\Delta t \approx 1710$ s) since the refined grid does not cover the polar regions. In addition, the speedup is also partly due to a fewer number of refined blocks in FV since an additional halo region is enforced in SEM. Furthermore, the table shows that the error norms are almost identical in the adapted and uniform grid runs. Therefore, the adaptive meshes offer computational savings over the uniform simulations in these passive advection runs.

b. Passive advection of a slotted cylinder

In our second advection example the cosine bell is replaced with a slotted cylinder. All other parameters and flow fields stay the same as discussed above. Such an advection test has recently been applied in spherical geometry by Nair et al. (2003), Lipscomb and Ringler (2005) and Jablonowski et al. (2006). The slotted cylinder exhibits very sharp non-smooth edges in comparison to the rather smoothly varying cosine bell. Therefore, it especially challenges the non-monotonic numerical scheme in SEM. The radius of the cylinder is set to $R = a \times \pi/4$ with a slot of total width $a \times \pi/4$ and length $a \times 3\pi/8$. This rather wide slotted cylinder is chosen to allow grid coarsenings within the slot. As in Lipscomb and Ringler (2005) and Jablonowski et al. (2006), the initial height of the cylinder is set to $h = 1000$ m, whereas h is set to zero for all $r > R$ and inside the slot. The long axis of the slot is perpendicular to the equator and the cylinder is initially centered at $(\lambda_c, \varphi_c) = (3\pi/2, 0)$. The flow orientation angle $\alpha = 30^\circ$ is selected that avoids any grid symmetries along the trajectory path.

The model is run for 12 days which completes a full revolution of the advected cylinder. As before, the initial conditions then serve as the analytic reference solution. Three refinement levels are used that start from a coarse $5^\circ \times 5^\circ$ base grid. This leads to a $0.625^\circ \times 0.625^\circ$ resolution within the refined area. Here, a grid-scale dependent adaptation criterion is applied that flags a block for refinement if the height difference between neighboring cells exceeds 10 m in the case of FV. For SEM, elements marked for refinement if the height exceeds 10 m.

Figure 6 shows snapshots of the adaptive SEM (left column) and FV (right column) simulations at model day 0, 6, 9 and 12. The height field with $h \geq 5$ m is shaded in gray with overlaid adapted elements and blocks. The grid is mainly refined along the sharp edges and inside the advected cylinder and kept coarse in distant domains. In FV, there is some minor numerical diffusion along the sharp edges which causes a slight broadening of the cylinder during the course of the simulation. The broadening can clearly be seen in Fig. 6h that shows a cross section of the slotted cylinder along the equator at day 12 together with its initial reference shape. There are no under- or overshoots in the monotonic FV model. This is in contrast to SEM that now exhibits significant under- and overshoots along the sharp edges with maximum amplitudes of ± 200 m (specific locations not shown). These Gibbs oscillations are documented in Figs. 6b-d. They lead to a wider refinement area that also captures the numerical ripples around the slotted cylinder. During the course of the SEM simulations, a different filtering constant was applied. In particular, the 12th order Boyd-Vandeven filter (Boyd 1996; Vandeven 1991) was applied at every time step with a convex combination update of 0.75 for the unfiltered solution and 0.25 for the filtered one. For all other shallow water tests discussed in this paper, the same 12th order filter was employed every five time steps with a convex combination of 0.95 and 0.05 for the unfiltered and filtered solution, respectively.

Despite the different numerical characteristics of the two models, the normalized height error norms of both SEM and FV simulations are comparable. The normalized $l_2(h)$ and $l_\infty(h)$ error norms after 12 days are 0.1895 and 0.7111 in SEM, and 0.1738 and 0.7532 in FV.

c. Steady-state geostrophic flow

Test case 2 is a steady-state zonal geostrophic flow, representing a balance between the Coriolis and geopotential gradient forces in the momentum equation. The initial velocity field on the sphere

is given by

$$u = u_0 (\cos \theta \cos \alpha + \cos \lambda \sin \theta \sin \alpha)$$

$$v = -u_0 \sin \lambda \sin \alpha .$$

where α is the angle between the axis of solid body rotation and the polar axis. The analytic geopotential field $\Phi = gh$ is specified as

$$\Phi = \Phi_0 - \left(a\Omega u_0 + \frac{u_0^2}{2} \right) \times (-\cos \lambda \cos \theta \sin \alpha + \sin \theta \cos \alpha)^2 .$$

a is the radius of the earth and Ω is the rotation rate. Parameter values are specified to be $u_0 = 2\pi a/(12 \text{ days})$ and $\Phi_0 = 2.94 \times 10^4 \text{ m}^2/\text{s}^2$. These fields also represent the analytic solution of the flow. The Coriolis parameter is given by

$$f = 2\Omega (-\cos \lambda \cos \theta \sin \alpha + \sin \theta \cos \alpha) .$$

We primarily use this large-scale flow pattern to assess the characteristics of the fine-coarse mesh interfaces in two statically adapted grid configurations. Both models SEM and FV utilize non-conforming meshes with a resolution jump by a factor of two in each direction at the interfaces. Note that the FV model requires interpolations in the ghost cell regions of neighboring blocks whenever the resolution is changed. This is not the case for SEM. In general, inserting a refined patch of elements (SEM) or blocks (FV) in a random location should result in either no changes in the error, if the flow is completely resolved, or in a small decrease in the overall error. Inserting the patch in a strategic location might even lower the error more significantly.

Here, we start our simulations from a uniform $2.5^\circ \times 2.5^\circ$ base grid which is given by 216 spectral elements with 6×6 GL points in SEM. In FV, this corresponds to the block data structure consisting of $12 \times 16 = 192$ blocks with 6×9 grid points in latitudinal and longitudinal direction, respectively. Two refinement levels are utilized which lead to the finest mesh spacing $0.625^\circ \times$

0.625° in both models.

In the first configuration, a refined patch of size $45^\circ \times 30^\circ$ (longitudes \times latitudes) is centered at (180°E, 45°N). This patch spans the approximate domain (157.5°E,30°N)-(202.5°E,60°N) which is indicated by the dotted contours for both models in Fig. 7. Here, the geopotential height fields of the FV and SEM simulations at day 14 are displayed which are both visually indistinguishable from the initial state. In the second configuration (not shown) a patch of identical size is centered at (135°E, 30°N). This covers the region between (112.5°E,15°N) - (157.5°E,45°N) which is characterized by strong gradients in the geopotential height field (see also the discussion in Jablonowski et al. (2004)). The two locations give insight into the dependency of the errors on the position of the refined patch.

Both statically adapted configurations are integrated for 14 days with $\alpha = 45^\circ$. As mentioned before this rotation angle represents the most challenging direction for both models due to the choice of the cubed-sphere geometry in SEM and the upwind-biased finite-volume algorithm in FV. The results for the l_2 normalized geopotential height errors for SEM and FV are reported in Fig. 8. It is expected that the errors in SEM are lower than in FV which is confirmed by Figs. 8a-b. This is due to the spectral convergence (SEM) of the smooth solution which is infinitely differentiable. In general, such spectral convergence cannot be archived by grid point models which typically exhibit higher error norms. Here it is interesting to note that the two refined patches in SEM lead to a slight decrease in the error in comparison to the uniform-mesh run (Fig. 8a). The errors are independent of the location of the refined area. This is in contrast to the error norms in FV (Fig. 8b). The refined patches introduce slight disturbances of the geostrophic balance and non-divergent wind field which now cause the error norms to increase in comparison to the uniform-mesh run. The increase is sensitive to the location of the refined patch. In particular, the errors in FV grow faster if the patch intersects the strong gradient regime in the geopotential height field (centered at (135°E, 30°N)). Despite this characteristic, the error is still in the expected range for grid point based models, as for example compared to Tolstykh (2002). The increase in error is mainly triggered by interpolations in the ghost cell regions and depends on the order of the interpolation scheme (see

also discussion in Jablonowski (2004)). Higher order schemes reduce the generation of spurious divergence patterns within the interpolated ghost cell regions which is the main error source in this non-divergent flow field.

d. Flow over an idealized mountain

Test case 5 of the Williamson et al. (1992) test suite is a zonal flow impinging on a mountain. The mean equivalent depth of the atmosphere is set to $h_0 = 5960$ m. The mountain height is given by $h_s = h_{s_0}(1 - r/R)$, where $h_{s_0} = 2000$ m, $R = \pi/9$, and $r^2 = \min[R^2, (\lambda - \lambda_c)^2 + (\theta - \theta_c)^2]$. The center of the mountain is located at $\lambda_c = 3\pi/2$ and $\theta_c = \pi/6$ in spherical coordinates. The test case is integrated for 15 model days with a $5^\circ \times 5^\circ$ base grid as in test case 1. In addition, three levels of static refinements are introduced where the height of the mountain is greater than 0 m. The corresponding initial grids for SEM and FV are shown in Figs. 9a, 9e and 2.

During the course of the simulation dynamic refinements with three refinement levels are applied whenever the absolute value of the relative vorticity ζ is greater than $2 \times 10^{-5} \text{ s}^{-1}$. This refinement criterion is evaluated every two hours in both FV and SEM. Grid coarsenings, on the other hand, are invoked in regions where the threshold is no longer met. Figure 9 shows the time evolution of the geopotential height field for both models at days 0, 5, 10 and 15. The adapted elements on the cubed sphere (SEM) and adapted blocks (FV) are overlaid. It can be seen that both models track the evolving lee-side wave train reliably and in the refinement regions are apparent. Overall, the refinements in SEM cover a broader area because a one-element wide halo was enforced around the regions marked for refinement. This option reduces the number of adaptation cycles but on the other hand increases the overall workload. The number of adapted elements in SEM and adapted blocks in FV at day 15 is also documented in Table 2. They almost differ by a factor of 2. Note, that SEM employs a 20 s time step, the time step for FV is 138 s.

The results can be quantitatively compared via normalized error norms which are shown in Fig. 10. An analytic solution is not known. Therefore, the normalized error metrics are computed by comparing the SEM and FV simulations to a T426 spectral transform reference solution.

The corresponding spectral shallow water model was developed at the National Center for Atmospheric Research (NCAR) (Jakob et al. 1993; Jakob-Chien et al. 1995). The high resolution reference solution was computed by the German Weather Service (DWD) and is available online (<http://icon.enes.org/swm/stswm/node5.html>) as an archived NetCDF data set with daily snapshots of the spectral transform simulation. The T426 spectral simulation utilized a Gaussian grid with 640×1280 grid points in latitudinal and longitudinal direction which corresponds to a grid spacing of about 31 km at the equator. Figure 10 compares the normalized l_2 height errors of the adaptive runs to uniform-resolution simulations. Both models are depicted. The errors in the uniform SEM runs decrease rapidly as the model resolution is increased (Fig. 10a). The rate of convergence lies between 2.4 and 2.8. The SEM adaptive run with three refinement levels matches the $1.25^\circ \times 1.25^\circ$ error trace very closely. The errors in the uniform FV simulations (Fig. 10 b) converge more slowly to the reference solution with a rate of convergence between 1.6 and 1.9. Here, the error trace of the FV adaptive simulation resembles the $2.5^\circ \times 2.5^\circ$ uniform run despite the higher resolution in the refined areas. It indicates that the coarser domains in FV still contribute considerably to the global l_2 error measure. In addition, the interpolations in the ghost cell regions add to the error norms.

The wall clock time needed to finish the adaptive 15-day simulations is comparable in both models. On one IBM POWER5+ processor, SEM finishes the simulation after 1503 s, FV finishes after 904 s. If the SEM haloing condition is removed, the wall clock time for the 15-day SEM run reduces to 1041 s. The reduction is mainly due to the reduced work load with a total of 996 adapted elements at day 15. Note that the corresponding l_2 error norm at day 15 in SEM is ten times lower than the l_2 errors in FV (Fig. 10).

In order to assess the AMR performance that could be expected in a dry 3D primitive-equation based dynamical core, we also ran the SEM model in a multi-level shallow water configuration. Such a configuration omits the additional work load required for the vertical advection and thermodynamic equation, but nevertheless gives a first estimate of the expected performance gains and parallel scaling properties. Table 5 shows the wall clock execution times for several 15-day

mountain wave simulations with 26 vertically stacked shallow water levels for 8, 16, and 24 IBM POWER5+ processors (with 1.9 GHz clock speed). The table lists the percentage of time spent in several components of the SEM AMR code. In particular, *flops* refers to the floating-point operations necessary to solve the shallow water equations, *comm* refers to the boundary data exchanges and *overhead* refers to costs related to the refinement and coarsening of the grid. The timing data are listed for both uniform $0.625^\circ \times 0.625^\circ$ resolution runs and the AMR simulations with a $5^\circ \times 5^\circ$ base grid and three refinement levels. Identical time steps were used. The AMR timing data show that the adaptive mesh simulations always run faster than the corresponding fixed resolution runs with FIXED/AMR timing ratios that lie between 3.9 and 2.2. The reduced parallel efficiency of the AMR runs for the SEM model with 16 and 24 processors is mainly due to increased overhead invoked by the management of the AMR grid and partly due to increased MPI (Message Passing Interface) communication costs. Despite this sub-optimal scaling, the 24-processor AMR run still decreases the time to solution considerably. Again, we note that neither model has not been tuned for performance or scalability, yet. This will be the subject of future research.

e. Rossby-Haurwitz wave

The initial condition for test case 6 of the Williamson et al. (1992) test suite is a wavenumber 4 Rossby-Haurwitz wave. These waves are analytic solutions to the nonlinear non-divergent barotropic vorticity equation, but not closed-form solutions of the barotropic shallow water equations. However, in a shallow water system the wave pattern moves from west to east without change of shape during the course of the integration. The initial conditions are fully described in Williamson et al. (1992), the orography field is set to zero. The Rossby-Haurwitz wave with wavenumber 4 exhibits extremely strong gradients in both the geopotential and the wind fields. This test is especially hard for the FV adaptive grid simulations due not only to the strong gradients but also to the dominant 45° transport angle of the flow in midlatitudes. This challenges the upwind-biased finite volume algorithm and has the potential to accentuate even minor errors.

Both shallow water models are integrated for 14 days on a $2.5^\circ \times 2.5^\circ$ base grid. This base reso-

lution is identical to test case 2. In addition, static refinements at refinement level 1 ($1.25^\circ \times 1.25^\circ$) are placed within eight pre-determined regions of interest. In particular, the grid is refined where the initial meridional wind field is $v \leq -60 \text{ m s}^{-1}$ which leads to an almost identical number of refined elements and blocks in the two models (Table 2). This rather arbitrary refinement criterion is intended to test whether the wavenumber 4 pattern moves smoothly through the refined grid patches. Only minor improvements of the l_2 error norms are expected as the solution is already well-resolved at the uniform $2.5^\circ \times 2.5^\circ$ resolution. The daily simulation results of SEM and FV are compared to a T511 spectral transform reference solution. As for test case 5 (flow over the mountain), the reference solution was computed by DWD using the NCAR shallow water model. The solutions are available online (<http://icon.enes.org/swm/stswm/node5.html>) as an archived NetCDF data set with daily snapshots of the spectral transform simulation ($\approx 26 \text{ km}$ resolution).

Figures 11a-b show the geopotential height field of the adaptive SEM and FV model runs at day 7. It can clearly be seen that both SEM and FV maintain the wavenumber 4 pattern of the height field rather well while moving through the refined patches. Here, the results can be visually compared to the spectral T511 reference solution (Fig. 11c). No noise or distortions are visible at this stage. However, FV develops slight asymmetries in the height field at later times. They originate at the interfaces of the refined areas and slightly disturb the wave field over the course of the integration. These perturbations can again be traced back to ghost cell interpolations in the FV model that now lead to a slight increase in the l_2 errors norm. The effect is amplified by the very strong gradients in the flow field and the dominant 45° transport angle. The time steps for these simulations are 15 s and 225 s for SEM and FV, respectively.

The error norms for both models are quantitatively compared in Fig. 12. The figure shows the time evolution of the normalized l_2 height error norms in comparison to fixed-resolution SEM and FV model runs. In particular, two different base resolutions are shown for SEM. These are the regular $2.5^\circ \times 2.5^\circ$ base grid (216 elements) and a coarser $3.2^\circ \times 3.2^\circ$ base mesh (96 elements). In both SEM cases, 6×6 GL quadrature points per spectral element are used. The coarser simulation

is added since SEM already converges rapidly to the reference solution with $2.5^\circ \times 2.5^\circ$. Figure 12 shows that SEM exhibits smaller errors than FV at the same uniform resolution. At day 12, the errors in the FV run are rather similar to the coarser 3.2° SEM simulation. With respect to the static adaptations, SEM does not show an increase in the error, in contrast to FV. Instead, the SEM errors in the statically adaptive runs are almost identical to the uniform-mesh simulation or slightly diminish at the end of the forecast period. Note that the error curves of the uniform and adaptive SEM $2.5^\circ \times 2.5^\circ$ simulations overlay each other and are therefore visually indistinguishable.

f. Evolution of a barotropic wave

To increase the complexity of the chosen test cases even further we also select the highly nonlinear barotropic instability test case as suggested by Galewsky et al. (2004). We choose the inviscid variant of the test without an explicit second-order diffusion mechanism. The test describes the rapid evolution of a barotropic wave in the northern midlatitudes that exhibits a continuous nonlinear transfer of energy from large to small scales. Sharp vorticity gradients develop over time which makes the test especially difficult for non-monotonic numerical schemes like SEM or Discontinuous Galerkin approaches. In these types of models the sharp gradients cause Gibbs oscillations that must be controlled by suitable filtering. In the FV model though, the monotonicity constraint acts as a local filter that provides sufficient dissipation.

The initial conditions are described in Galewsky et al. (2004). In brief, the models are initialized with zonally symmetric initial conditions that prescribe a strong zonal jet in the northern midlatitudes as well as a geostrophically balanced height distribution. The smooth height field is then overlaid with a local small-amplitude height perturbation in the center of the jet stream. This triggers the evolution of a barotropic wave over the course of several days. An analytic solution is not known. Therefore, we provide snapshots of high-resolution reference solutions for comparison purposes. In particular, Fig. 13 shows a convergence study at day 6 for both SEM and FV. In these model runs, we continuously decrease the uniform horizontal resolutions to span the range from $5^\circ \times 5^\circ$ to $0.3125^\circ \times 0.3125^\circ$. The figure depicts the relative vorticity field at day 6. It is evident

that SEM does not capture the solution at the two coarsest resolutions but rather shows the evolution of a wave number 4 signal invoked by the computational cubed-sphere mesh. Even the SEM $1.25^\circ \times 1.25^\circ$ simulation displays a weak wave number 4 effect. Similar grid phenomena can also be found in triangular icosahedron-based grids at coarse resolutions, as for example demonstrated by Jablonowski and Williamson (2006b,a) in 3D baroclinic wave studies. The grid effect is overly enhanced by this zonally symmetric initial setup and furthermore, less important if real atmospheric circulations are assessed.

FV does not capture any wave solution at $5^\circ \times 5^\circ$ but starts to form the barotropic wave at $2.5^\circ \times 2.5^\circ$. In both models, $1.25^\circ \times 1.25^\circ$ and higher resolutions are needed to simulate the barotropic instability reliably. The barotropic wave tends to converge, at least visually, at the two highest resolutions considered here. Again note that none of the models applies the strong explicit second-order diffusion mechanism originally suggested by Galewsky et al. (2004). Therefore, very minor differences at the smallest scales are expected and apparent in the high-resolution SEM and FV simulations which closely resemble each other at day 6. The main difference is the small-scale noise that SEM exhibits at $1.25^\circ \times 1.25^\circ$ and $0.625^\circ \times 0.625^\circ$. This noise diminishes at the higher resolutions. In addition, SEM shows stronger vorticity maxima in the thin vorticity filaments (white contours). The SEM vorticity maxima reach $\approx 20 \times 10^{-5} \text{ s}^{-1}$, they are around $15.5 \times 10^{-5} \text{ s}^{-1}$ in FV. These values do not suggest that SEM has an effective better resolution due to possible oscillations and overshoots in SEM's non-monotonic algorithm. The high resolution results can also be compared to the inviscid T341 spectral transform solutions shown in Galewsky et al. (2004) where the relative vorticity at day 6 increases with respect to spatial resolution. Despite the considerable Gibbs oscillations in the spectral approach the general structure of the relative vorticity field at day 6 is comparable to SEM and FV. Note that the smallest scales are controlled by the internal dissipation mechanisms and filters in SEM and FV. As mentioned above these are the filtering operations in SEM which is comparable to removing the aliasing effects at the element level, and the monotonicity constraint, the divergence damping, and the polar Fourier and algebraic 3-point (digital) filtering mechanisms in FV.

For our adaptive simulations we select the vorticity-based dynamic refinement criterion $|\zeta| \geq 3 \times 10^{-5} \text{ s}^{-1}$. This refinement criterion flags the whole zonal jet region for refinement at the initial state. Both models are re-initialized to guarantee an improved initial representation of the zonal jet area. Figure 14 shows four snapshots of the adaptive SEM and FV simulations with four refinement levels and overlaid adapted elements and blocks. Both models start with a coarse $5^\circ \times 5^\circ$ resolution so that the smallest block sizes represent a $0.3125^\circ \times 0.3125^\circ$ grid. The refined areas closely track the evolving barotropic wave that develops rapidly after model day 4. This is demonstrated by the newly refined spectral elements and blocks that overall cover very similar regions. At day 6 the barotropic wave has formed mature vortices and thin vorticity filaments that are present in both the adapted and uniform runs. It can be seen that the adapted SEM and FV simulations converge towards the high-resolution reference solutions as depicted in Figs. 13e and j. The differences between the adaptive SEM and FV solutions are very small.

5. Conclusions

In this paper, two shallow water models with adaptive mesh refinement capabilities were compared. The models are an interpolation-based spectral element model (SEM) on a cubed-sphere grid and a conservative and monotonic finite volume model (FV) in latitude-longitude geometry. Both adaptive mesh approaches utilize a quad-tree AMR technique that reduces the mesh spacings by a factor of two during each refinement step. Coarsenings reverse this adaptations principle. Then four “children/leaves” are coalesced which doubles the grid distances. In SEM, the refinement strategy targets the spectral elements which contain additional Gauss-Legendre and Gauss-Lobatto-Legendre collocation points for scalar and vector components. In FV, the adaptations are applied to a block-data structure in spherical coordinates which consists of a fixed (self-similar) block size. These blocks are surrounded by ghost cell regions which require interpolation and averaging procedures at fine-coarse mesh interfaces. No ghost cells areas are needed in SEM. In both models neighboring elements or blocks can only differ by one refinement level. This leads to

cascading and non-conforming refinement regions around the finest mesh.

The models are compared via selected test cases from the standard Williamson et al. (1992) shallow water test suite and via a barotropic instability test. These tests comprise the passive advection of a cosine bell (test 1) and slotted cylinder, a steady-state geostrophic flow (test 2), a flow over an idealized mountain (test 5), a Rossby-Haurwitz wave (test 6) and the evolution of a growing barotropic wave. Static and dynamics adaptations are assessed which reveal the strengths and weaknesses of the AMR approaches. The AMR simulations show that both models successfully place static and dynamic adaptations in local regions without requiring a fine grid in the global domain. The adaptive grids reliably track the user-selected features of interests without visible distortions or noise at the mesh interfaces. In particular, three dynamic refinement criteria were evaluated. Among them were a simple geopotential height threshold (test 1), a gradient-based criterion that assessed the height differences between neighboring cells (slotted cylinder) as well as the magnitude of the relative vorticity (test 5 and barotropic instability). In the mountain wave simulations, the latter criterion successfully steered the SEM and FV refined grids into the Southern Hemisphere at the end of the 15-day forecast period. It also reliably detected the growing barotropic wave in the Northern Hemisphere and tracked the evolving vortices. The adaptive simulations closely matched the high-resolution reference solutions. In addition, two static AMR configurations in user-determined regions of interest were tested using test case 2 and 6 of the shallow water test suite. They confirmed that the flows move smoothly through the refined areas in both SEM and FV. Nevertheless, the FV simulations showed that small errors originate at fine-coarse grid interfaces. These errors were due to the interpolation and averaging mechanisms in the ghost cell regions of the block-data structure. This was not the case in SEM which exhibited a decrease in error whenever adaptations were introduced.

Overall, the number of dynamically refined elements or blocks was comparable in both models if the adaptations were confined to the equatorial or midlatitudinal regions. In polar regions though, the number of refined blocks in FV exceeded the number of refined elements in SEM considerably due to the convergence of the meridians in the latitude-longitude grid. In general, it was shown that

SEM exhibited smaller errors than FV for almost all test cases at identical resolutions. This is expected for SEM's high-order numerical technique despite its non-conservative and non-monotonic nature. The latter causes spurious oscillations and negative values for positive-definite fields (test 1 and the slotted cylinder). This was clearly demonstrated by the transport of the slotted cylinder that showed severe under- and overshoots near the sharp edges of the cylinder. Furthermore, slightly more filtering operations were applied in SEM. Such oscillations are non-existing in the mass-conservative and monotonic FV model which, on the other hand, introduces numerical dissipation through its monotonicity constraint. This dissipation is reduced at high resolutions. Then the nonlinear SEM and FV simulations resemble each other very closely which raises questions about the computational efficiencies.

The computational efficiency of both SEM and FV with uniform and adapted meshes was briefly discussed for selected advection tests (test case 1) and the flow over an idealized mountain (test case 5). Overall, the single processor AMR simulations always offer a performance gain in comparison to uniform, globally refined grids while showing almost identical error measures. However, the AMR speed-ups assessed in our advection examples (test 1) varied greatly with a range of 6-123. In FV, they strongly depended on the rotation angle which determines the maximum allowable time step. In SEM, the speed-up was almost independent of the rotation angle since identical time steps were used. Then the speed-up is exclusively due to the reduced work load in the adaptive simulation despite the additional overhead that AMR invokes. A parallel performance and scale analysis for SEM was also performed (test case 5). It showed that the parallel overhead can become significant which leaves room for future improvements and research.

The non-conservation problem and the removal of some of the Gibbs oscillations in SEM have recently been addressed (Mark Taylor et al., poster at the 12th Annual Community Climate System Model Workshop, Breckenridge, CO, 19-21 June 2007). In addition, the use of the Discontinuous Galerkin formulation decreases the communication on parallel computer architectures and therefore, has the potential to diminish the cost of the AMR communication overhead. Future developments will include an evaluation of the DG method as well as efficient time-stepping tech-

niques (Nair et al. 2005; St-Cyr and Thomas 2005b,a; St-Cyr 2006) to avoid the very small time steps for numerical stability. Furthermore, tests involving unsteady analytical solutions such as the examples in Läuter et al. (2005), effects of orography with optimal filtering, and an adaptive 3D dynamical core intercomparison will be the subject of interesting future research.

Acknowledgments. The authors thank Paul Fischer and Duane Rosenberg for many insightful discussions on adaptive spectral elements methods. This work was partially supported by an NSF collaborations in mathematics and the geosciences grant (022282) and the DOE climate change prediction program (CCPP). In addition, CJ was partly supported by NASA Headquarters under the Earth System Science Fellowship Grant NGT5-30359. We also wish to thank the reviewers for their suggestions that greatly improved the manuscript.

References

- Bacon, D. P., N. N. Ahmad, Z. Boybeyi, T. J. Dunn, M. S. Hall, P. C. S. Lee, R. A. Sarma, M. D. Turner, K. T. W. III, S. H. Young, and J. W. Zack, 2000: A dynamically adapting weather and dispersion model: The operational multiscale environment model with grid adaptivity (OMEGA). *Mon. Wea. Rev.*, **128**, 2044–2076.
- Behrens, J., 2006: *Adaptive Atmospheric Modeling - Key techniques in grid generation, data structures, and numerical operations with applications*. Springer, Lecture Notes in Computational Science and Engineering, ISBN 3-540-33382-7, 207 pp.
- Behrens, J., N. Rakowsky, W. Hiller, D. Handorf, M. Läuter, J. Pöpke, and K. Dethloff, 2005: amatos: Parallel adaptive mesh generator for atmospheric and oceanic simulation. *Ocean Modelling*, **10**, 171–183.
- Boyd, J. P., 1996: The Erfc-Log filter and the asymptotics of the Euler and Vandeven sequence accelerations. *Proceedings of the Third International Conference on Spectral and High Order Methods*, A. V. Ilin and L. R. Scott, eds., Third International Conference on Spectral and High Order Methods, Houston Journal of Mathematics, 267–276.
- 2004: Book review: High-order methods for incompressible fluid flow. *SIAM Rev.*, **46**, 151–157.
- Carpenter, R. L., K. K. Droegemeier, P. R. Woodward, and C. E. Hane, 1990: Application of the Piecewise Parabolic Method (PPM) to meteorological modeling. *Mon. Wea. Rev.*, **118**, 586–612.
- Colella, P. and P. R. Woodward, 1984: The Piecewise Parabolic Method (PPM) for gas-dynamical simulations. *J. Comput. Phys.*, **54**, 174–201.
- Dennis, J. M., 2003: Partitioning with space-filling curves on the cubed sphere. *Proc. International Parallel and Distributed Processing Symposium (IPDPS)*, IEEE/ACM, Nice, France, CD-ROM. No. 269a.

- Deville, M. O., P. F. Fischer, and E. H. Mund, 2002: *High-Order Methods for Incompressible Fluid Flow*. Number 9 in Cambridge Monographs on Applied and Computational Mathematics, Cambridge University Press, 528 pp.
- Dietachmayer, G. S. and K. K. Droegemeier, 1992: Application of continuous dynamic grid adaptation techniques to meteorological modeling. Part I: Basic formulation and accuracy. *Mon. Wea. Rev.*, **120**, 1675–1706.
- Feng, H. and C. Mavriplis, 2002: Adaptive spectral element simulations of thin flame sheet deformations. *J. Sci. Comput.*, **17**, 1–3.
- Fischer, P. F., G. Kruse, and F. Loth, 2002: Spectral element methods for transitional flows in complex geometries. *J. Sci. Comput.*, **17**, 81–98.
- Fournier, A., M. A. Taylor, and J. J. Tribbia, 2004: The spectral element atmosphere model (SEAM): High-resolution parallel computation and localized resolution of regional dynamics. *Mon. Wea. Rev.*, **132**, 726–748.
- Fox-Rabinovitz, M. S., J. Coté, B. Dugas, M. Déqué, and M. J. McGregor, 2006: Variable resolution general circulation models: Stretched-grid model intercomparison project (SGMIP). *J. Geophys. Res.*, **111**, doi:10.1029/2005JD006520.
- Frohn, L. M., J. H. Christensen, and J. Brandt, 2002: Development of a high-resolution nested air pollution model – the numerical approach. *J. Comput. Phys.*, **179**, 68–94.
- Galewsky, J., R. K. Scott, and L. M. Polvani, 2004: An initial-value problem for testing numerical models of the global shallow water equations. *Tellus, A*, **56**, 429–440.
- Gibbs, J. W., 1899: Fourier Series. *Nature*, **59**, 606.
- Giraldo, F. X., 2000: The Lagrange-Galerkin method for the two-dimensional shallow water equations on adaptive grids. *Int. J. Numer. Meth. Fluids*, **33**, 789–832.

- 2001: A spectral element shallow water model on spherical geodesic grids. *Int. J. Numer. Meth. Fluids*, **35**, 869–901.
- 2006: High-order triangle-based discontinuous Galerkin methods for hyperbolic equations on a rotating sphere. *J. Comput. Phys*, **214**, 447–465.
- Giraldo, F. X. and T. Warburton, 2005: A nodal triangle-based spectral element method for the shallow water equations on the sphere. *J. Comput. Phys.*, **207**, 129–150.
- Gopalakrishnan, S. G., D. P. Bacon, N. N. Ahmad, Z. Boybeyi, T. J. Dunn, M. S. Hall, Y. Jin, P. C. S. Lee, D. E. Mays, R. V. Madala, A. Sarma, M. D. Turner, and T. R. Wait, 2002: An operational multiscale hurricane forecasting system. *Mon. Wea. Rev.*, **130**, 1830–1847.
- Haidvogel, D., E. Curchitser, M. Iskandarani, R. Hughes, and M. Taylor, 1997: Global modeling of the ocean and atmosphere using the spectral element method. *Atmos.-Ocean*, **35**, 505.
- Iselin, J., W. J. Gutowski, and J. M. Prusa, 2005: Tracer advection using dynamic grid adaptation and MM5. *Mon. Wea. Rev.*, **133**, 175–187.
- Iselin, J., J. M. Prusa, and W. J. Gutowski, 2002: Dynamic grid adaptation using the MPDATA scheme. *Mon. Wea. Rev.*, **130**, 1026–1039.
- Jablonowski, C., 2004: *Adaptive Grids in Weather and Climate Modeling*. Ph.D. dissertation, University of Michigan, Ann Arbor, MI, Department of Atmospheric, Oceanic and Space Sciences, 292 pp.
- Jablonowski, C., M. Herzog, J. E. Penner, R. C. Oehmke, Q. F. Stout, and B. van Leer, 2004: Adaptive grids for weather and climate models. *ECMWF Seminar Proceedings on Recent Developments in Numerical Methods for Atmosphere and Ocean Modeling*, ECMWF, Reading, United Kingdom, 233–250.

- Jablonowski, C., M. Herzog, J. E. Penner, R. C. Oehmke, Q. F. Stout, B. van Leer, and K. G. Powell, 2006: Block-structured adaptive grids on the sphere: Advection experiments. *Mon. Wea. Rev.*, **134**, 3691–3713.
- Jablonowski, C. and D. L. Williamson, 2006a: A baroclinic instability test case for atmospheric model dynamical cores. *Quart. J. Roy. Meteor. Soc.*, **132**, 2943–2975.
- 2006b: A baroclinic wave test case for dynamical cores of General Circulation Models: Model intercomparisons. NCAR Tech. Note NCAR/TN-469+STR, National Center for Atmospheric Research, Boulder, Colorado, 89 pp.
- Jakob, R., J. J. Hack, and D. L. Williamson, 1993: Solutions to the shallow-water test set using the spectral transform method. Technical Report NCAR/TN-388+STR, National Center for Atmospheric Research, Boulder, Colorado.
- Jakob-Chien, R., J. J. Hack, and D. L. Williamson, 1995: Spectral transform solutions to the shallow water test set. *Journal of Computational Physics*, **119**, 164–187.
- Karypis, G., K. Schloegel, and V. Kumar, 2002: *ParMetis: Parallel Graph Partitioning and Sparse Matrix Ordering Library, Version 3.0*. University of Minnesota.
- Kurihara, Y. and M. A. Bender, 1980: Use of a movable nested-mesh model for tracking a small vortex. *Mon. Wea. Rev.*, **108**, 1792–1809.
- Kurihara, Y., G. J. Tripoli, and M. A. Bender, 1979: Design of a movable nested-mesh primitive equation model. *Mon. Wea. Rev.*, **107**, 239–249.
- Läuter, M., 2004: *Großräumige Zirkulationsstrukturen in einem nichtlinearen adaptiven Atmosphärenmodell*. Ph.D. dissertation, Universität Potsdam, Germany, Wissenschaftsdisziplin Physik der Atmosphäre, 135 pp.
- Läuter, M., D. Handorf, and K. Dethloff, 2005: Unsteady analytical solutions of the spherical shallow water equations. *J. Comput. Phys.*, **210**, 535–553.

- Läuter, M., D. Handorf, N. Rakowsky, J. Behrens, S. Frickenhaus, M. Best, K. Dethloff, and W. Hiller, 2007: A parallel adaptive barotropic model of the atmosphere. *J. Comput. Phys.*, **223**, 609–628.
- Lin, S.-J. and R. B. Rood, 1996: Multidimensional flux-form semi-Lagrangian transport scheme. *Mon. Wea. Rev.*, **124**, 2046–2070.
- 1997: An explicit flux-form semi-Lagrangian shallow water model on the sphere. *Quart. J. Roy. Meteor. Soc.*, **123**, 2477–2498.
- Lipscomb, W. H. and T. D. Ringler, 2005: An incremental remapping transport scheme on a spherical geodesic grid. *Mon. Wea. Rev.*, **133**, 2335–2350.
- Mavriplis, C., 1989: *Nonconforming Discretizations and a Posteriori Error Estimators for Adaptive Spectral Element Techniques*. Ph.D. dissertation, MIT, Boston, MA., 156 pp.
- Nair, R. D. and B. Machenhauer, 2002: The mass-conservative cell-integrated semi-Lagrangian advection scheme on the sphere. *Mon. Wea. Rev.*, **130**, 649–667.
- Nair, R. D., J. S. Scroggs, and F. H. M. Semazzi, 2003: A forward-trajectory global semi-Lagrangian transport scheme. *J. Comput. Phys.*, **190**, 275–294.
- Nair, R. D., S. J. Thomas, and R. D. Loft, 2005: A discontinuous Galerkin global shallow water model. *Mon. Wea. Rev.*, **133**, 876–888.
- Oehmke, R. C., 2004: *High Performance Dynamic Array Structures*. Ph.D. dissertation, University of Michigan, Ann Arbor, MI, 93 pp.
- Oehmke, R. C. and Q. F. Stout, 2001: Parallel adaptive blocks on a sphere. *Proc. 10th SIAM Conference on Parallel Processing for Scientific Computing*, SIAM, Portsmouth, VA, CD-ROM.
- Patera, A. T., 1984: A spectral element method for fluid dynamics: Laminar flow in a channel expansion. *J. Comput. Phys.*, **54**, 468–488.

- Prusa, J. M. and P. K. Smolarkiewicz, 2003: An all-scale anelastic model for geophysical flows: Dynamic grid deformation. *J. Comput. Phys.*, **190**, 601–622.
- Quarteroni, A. and A. Valli, 1997: *Numerical Approximations of Partial Differential Equations*, volume 23 of *Springer Series in Computational Mathematics*. Springer-Verlag, 544 pp.
- Rosenberg, D., A. Fournier, P. Fischer, and A. Pouquet, 2006: Geophysical–astrophysical spectral-element adaptive refinement (GASpAR): Object-oriented h-adaptive fluid dynamics simulation. *J. Comput. Phys.*, **215**, 59–80.
- Sadourny, R., 1972: Conservative finite-difference approximations of the primitive equations on quasi-uniform spherical grids. *Mon. Wea. Rev.*, **100**, 136–144.
- Skamarock, W. C., 1989: Truncation error estimates for refinement criteria in nested and adaptive models. *Mon. Wea. Rev.*, **117**, 872–886.
- Skamarock, W. C. and J. B. Klemp, 1993: Adaptive grid refinement for twodimensional and three-dimensional nonhydrostatic atmospheric flow. *Mon. Wea. Rev.*, **121**, 788–804.
- Skamarock, W. C., J. Olinger, and R. L. Street, 1989: Adaptive grid refinement for numerical weather prediction. *J. Comput. Phys.*, **80**, 27–60.
- Smolarkiewicz, P. K., 2006: Multidimensional positive definite advection transport algorithm: An overview. *Int. J. Num. Meth. Fluids*, **50**, 1123–1144.
- Smolarkiewicz, P. K. and J. Szmelter, 2005: MPDATA: An edge-based unstructured-grid formulation. *J. Comput. Phys.*, **206**, 624–649.
- St-Cyr, A., 2006: Operator splitting for high-order adaptive mesh refinement on the sphere. *Proceedings of the KSIAM 2006 spring meeting, Daegu, Korea*, S. D. Kim, ed., KSIAM, 1–6.
- St-Cyr, A. and S. J. Thomas, 2005a: Nonlinear OIFS for a hybrid Galerkin atmospheric model.

- Lecture Notes in Computer Science*, Springer-Verlag, volume LNCS 3516 of *Lecture Notes in Computer Science*, 57–63.
- 2005b: Nonlinear operator-integration factor splitting for the shallow water equations. *Appl. Numer. Math.*, **52**, 429–448.
- Taylor, M., J. Tribbia, and M. Iskandarani, 1997: The spectral element method for the shallow water equations on the sphere. *J. Comput. Phys.*, **130**, 92–108.
- Thomas, S. J. and R. D. Loft, 2002: Semi-implicit spectral element atmospheric model. *J. Sci. Comput.*, **17**, 339–350.
- Tolstykh, M. A., 2002: Vorticity-divergence semi-Lagrangian shallow-water model of the sphere based on compact finite differences. *J. Comput. Phys.*, **179**, 180–200.
- Tufo, H. M., 1998: *Algorithms for large-scale parallel simulations of unsteady incompressible flows in three-dimensional complex geometries*. Ph.D. dissertation, Brown University, Providence, R.I., 137 pp.
- Vandeven, H., 1991: Family of spectral filters for discontinuous problems. *J. Sci. Comput.*, **6**, 159–192.
- Wilhelm, D. and L. Kleiser, 2000: Stable and unstable formulation of the convection operator in spectral element simulations. *Appl. Numer. Math.*, **33**, 275–280.
- Williamson, D. L., J. B. Drake, J. J. Hack, R. Jakob, and P. N. Swarztrauber, 1992: A standard test set for numerical approximations to the shallow water equations in spherical geometry. *J. Comput. Phys.*, **102**, 211–224.

List of Figures

- 1 Positions of the Gauss-Legendre-Lobatto (GLL, circles) and Gauss-Legendre (GL, open squares) quadrature points on the spectral reference element with mapped coordinates ξ and η . There are 8 GLL velocity points and 6 GL scalar points in each direction which leads to the polynomial degrees 7 (GLL) and 5 (GL). 44
- 2 Adaptive grids on the sphere in (a) SEM and (b) FV. The adapted elements on the cubed-sphere (SEM) and adapted blocks in latitude-longitude geometry (FV) refine an idealized mountain as indicated by the contour lines. 45
- 3 Snapshots of the cosine bell (test case 1) with rotation angle $\alpha = 45^\circ$ and three refinement levels at day 3, 6, 9 and 12. The finest grid spacing is $0.625^\circ \times 0.625^\circ$, the adapted spectral elements (SEM) and blocks (FV) are overlaid. Left column (a-d) shows the SEM model, right column (e-h) depicts the FV model. The contour interval is 100 m, the zero contour is omitted. 46
- 4 Time traces of the normalized l_1 , l_2 and l_∞ geopotential height error norms for the cosine bell advection test (test case 1) with $\alpha = 45^\circ$. The (a) SEM and (b) FV advection models utilized three refinement levels that correspond to the finest grid resolution $0.625^\circ \times 0.625^\circ$. Note that the scales in (a) and (b) differ by a factor of 10. 47
- 5 North-polar stereographic projection of the cosine bell (test case 1) with rotation angle $\alpha = 90^\circ$ and three refinement levels at day 3 for (a) SEM and (b) FV. The finest grid spacing is $0.625^\circ \times 0.625^\circ$, the adapted spectral elements (SEM) and blocks (FV) are dotted. The contour interval is 100 m, the zero contour is omitted. . 48

6	Advection of a slotted cylinder with rotation angle $\alpha = 30^\circ$ and three refinement levels ($0.625^\circ \times 0.625^\circ$) in the models SEM (left column) and FV (right column). The height field with $h \geq 5$ m is shaded in gray. (a, e) Initial height field ($h = 1000$ m), (b, f) height field at day 6 (half a revolution), and (c, g) day 9. (d, h) Cross section of h along the equator at day 12 (full revolution). The adapted spectral elements (SEM) and blocks (FV) are overlaid.	49
7	Geopotential height field for test case 2 with $\alpha = 45^\circ$ at day 14 as simulated with the models (a) SEM and (b) FV. The statically adapted blocks with 2 refinement levels are overlaid (dotted contour). The refined patch is centered at ($180^\circ\text{E}, 45^\circ\text{N}$), the finest grid spacing is $0.625^\circ \times 0.625^\circ$. The contour interval is 200 m.	50
8	Time traces of the normalized l_2 geopotential height error norms for the steady state geostrophic flow (test case 2) with rotation angle $\alpha = 45^\circ$. Two simulations with static refinement regions centered at ($180^\circ\text{E}, 45^\circ$) and ($135^\circ\text{E}, 30^\circ$) are compared to a uniform $2.5^\circ \times 2.5^\circ$ resolution run. The adaptive (a) SEM and (b) FV model runs start with a $2.5^\circ \times 2.5^\circ$ base grid with two refinement level (finest grid resolution is $0.625^\circ \times 0.625^\circ$.)	51
9	Snapshots of the geopotential height field (test case 5, flow over a mountain) with three refinement levels at day 0, 5, 10 and 15. The finest grid spacing is $0.625^\circ \times 0.625^\circ$, the adapted spectral elements (SEM) and blocks (FV) are overlaid. Left column (a-d) shows the SEM model, right column (e-h) depicts the FV model. The refinement criterion is $ \zeta \geq 2 \times 10^{-5} \text{ s}^{-1}$. The contour interval is 100 m.	52
10	Time traces of the normalized l_2 geopotential height error norms for the flow over a mountain (test case 5). The adaptive simulations with three refinement levels ($0.625^\circ \times 0.625^\circ$ at the finest level) and several uniform-resolution runs are compared to a T426 spectral transform reference solution.	53

11	Snapshots of the geopotential height field of the Rossby-Haurwitz wave (test case 6) at day 7 for (a) SEM, (b) FV and (c) the T511 spectral model (reference solution, NCAR model). SEM and FV utilize an adaptive grid with one level of static adaptations. The base resolution is $2.5^\circ \times 2.5^\circ$ and $1.25^\circ \times 1.25^\circ$ within the refined region. The adapted elements (SEM) and blocks (FV) are overlaid. The contour interval is 250 m.	54
12	Time traces of the normalized l_2 geopotential height error norms for the Rossby-Haurwitz wave (test case 6). The statically adaptive simulations with one refinement levels ($1.25^\circ \times 1.25^\circ$ at the finest level) and several SEM and FV uniform-resolution runs are compared to a T511 spectral transform reference solution. The uniform and adaptive SEM $2.5^\circ \times 2.5^\circ$ errors overlay each other.	55
13	Barotropic wave at day 6 in the models SEM (left column) and FV (right column) with uniform (non-adapted) grids at increasing resolutions as indicated above. The relative vorticity field ζ in the Northern Hemisphere is shown.	56
14	Evolution of a growing barotropic wave in SEM (left column) and FV (right column) with four refinement levels (finest resolution is $0.3125^\circ \times 0.3125^\circ$). Snapshots of the relative vorticity field ζ at (a, e) day 3, (b, f) day 4, (c, g) day 5, and (d, h) day 6. The refinement criterion is $ \zeta \geq 3 \times 10^{-5} \text{ s}^{-1}$, the adapted spectral elements (SEM) and blocks (FV) are overlaid.	57

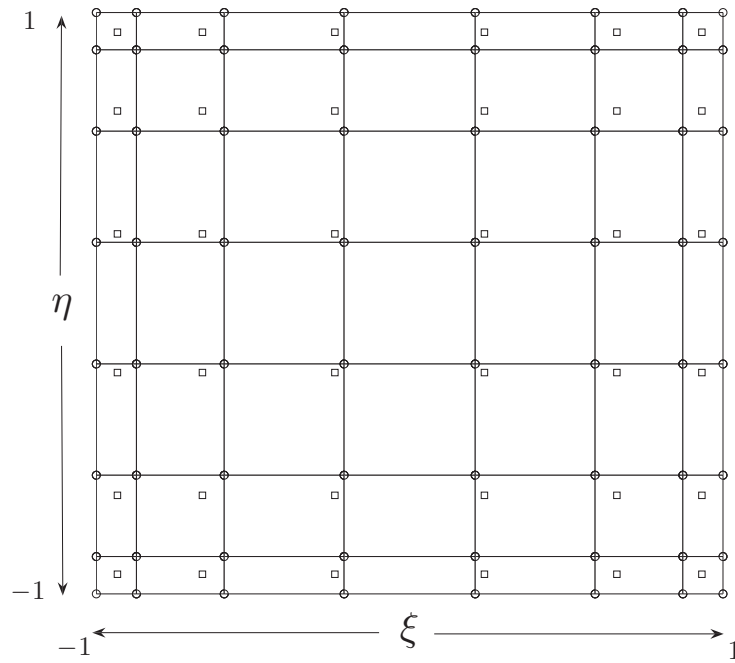
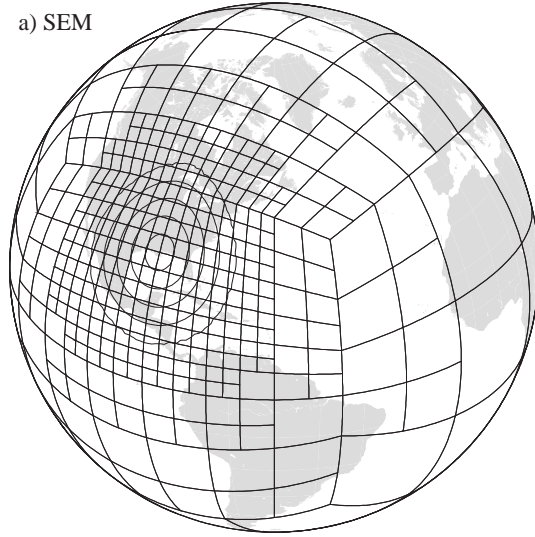


FIG. 1: Positions of the Gauss-Legendre-Lobatto (GLL, circles) and Gauss-Legendre (GL, open squares) quadrature points on the spectral reference element with mapped coordinates ξ and η . There are 8 GLL velocity points and 6 GL scalar points in each direction which leads to the polynomial degrees 7 (GLL) and 5 (GL).

a) SEM



b) FV

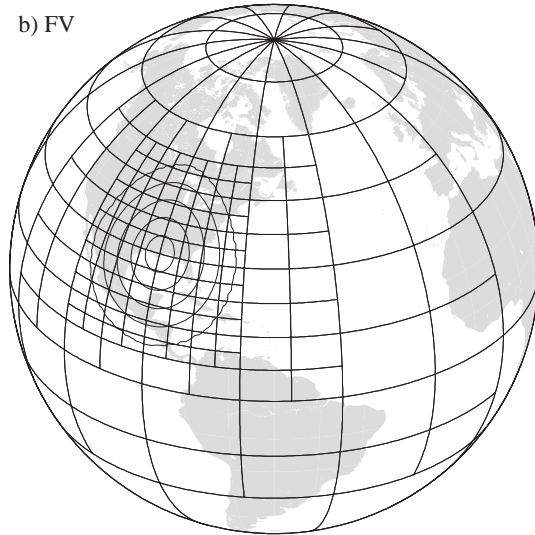


FIG. 2: Adaptive grids on the sphere in (a) SEM and (b) FV. The adapted elements on the cubed-sphere (SEM) and adapted blocks in latitude-longitude geometry (FV) refine an idealized mountain as indicated by the contour lines.

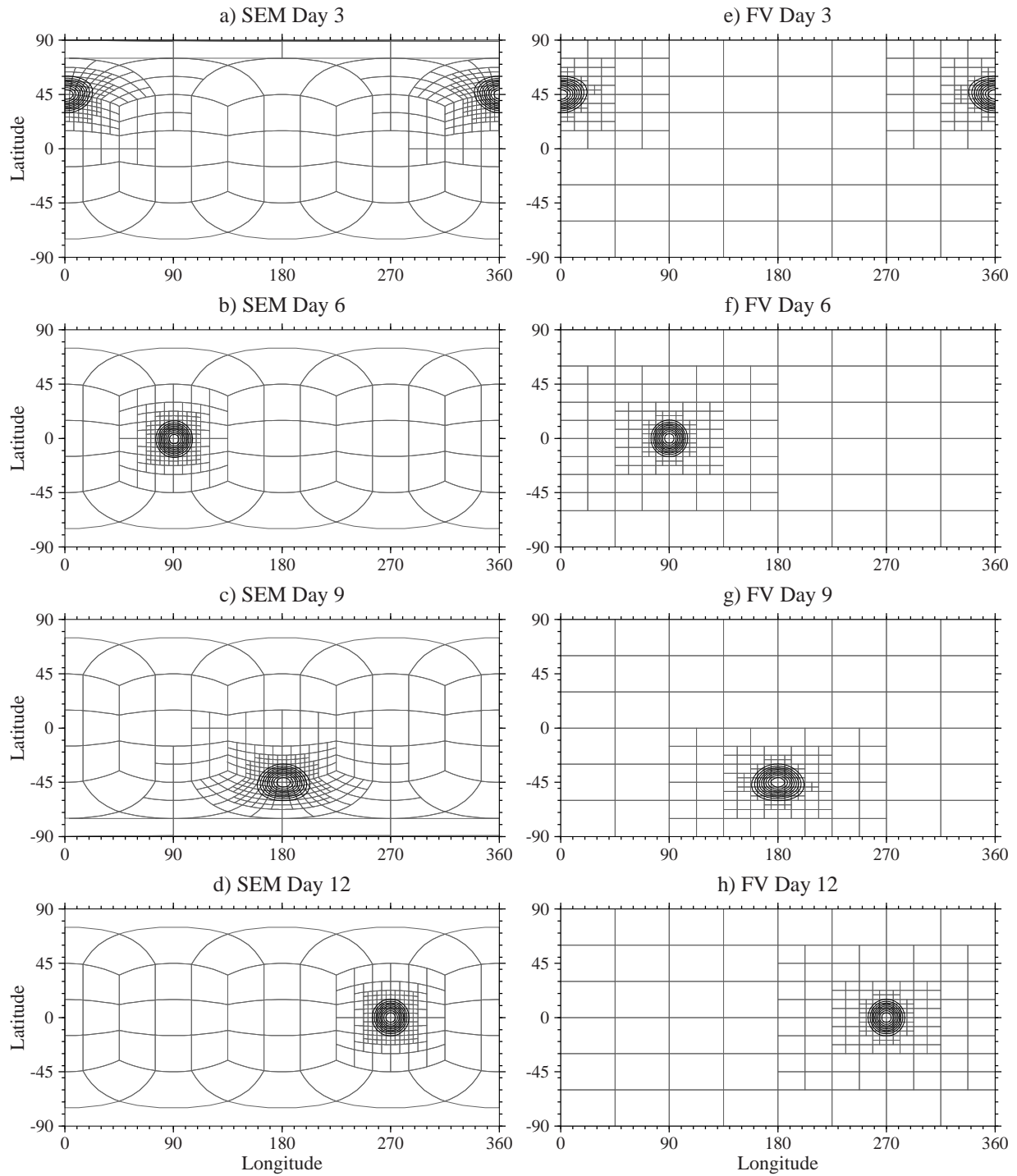


FIG. 3: Snapshots of the cosine bell (test case 1) with rotation angle $\alpha = 45^\circ$ and three refinement levels at day 3, 6, 9 and 12. The finest grid spacing is $0.625^\circ \times 0.625^\circ$, the adapted spectral elements (SEM) and blocks (FV) are overlaid. Left column (a-d) shows the SEM model, right column (e-h) depicts the FV model. The contour interval is 100 m, the zero contour is omitted.

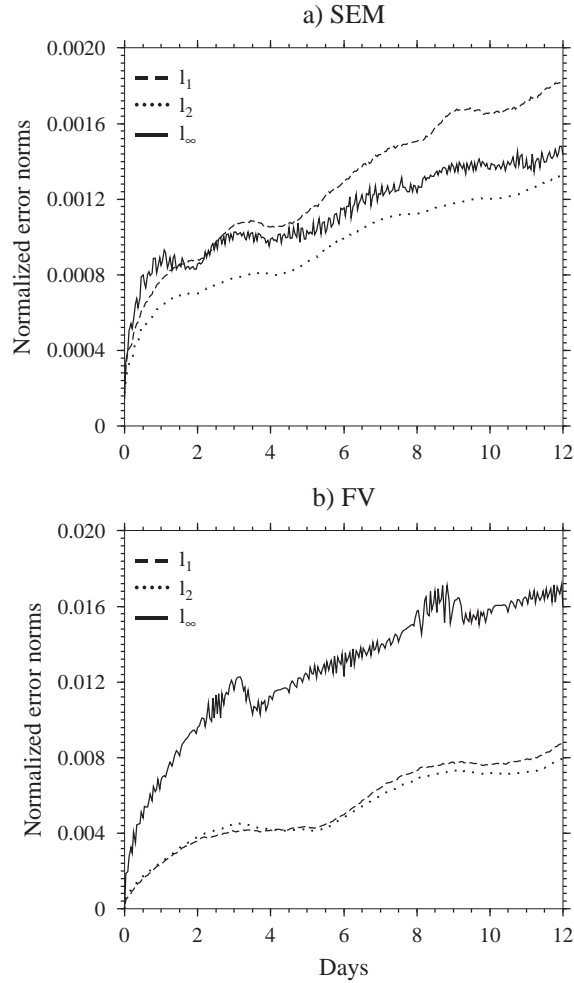


FIG. 4: Time traces of the normalized l_1 , l_2 and l_∞ geopotential height error norms for the cosine bell advection test (test case 1) with $\alpha = 45^\circ$. The (a) SEM and (b) FV advection models utilized three refinement levels that correspond to the finest grid resolution $0.625^\circ \times 0.625^\circ$. Note that the scales in (a) and (b) differ by a factor of 10.

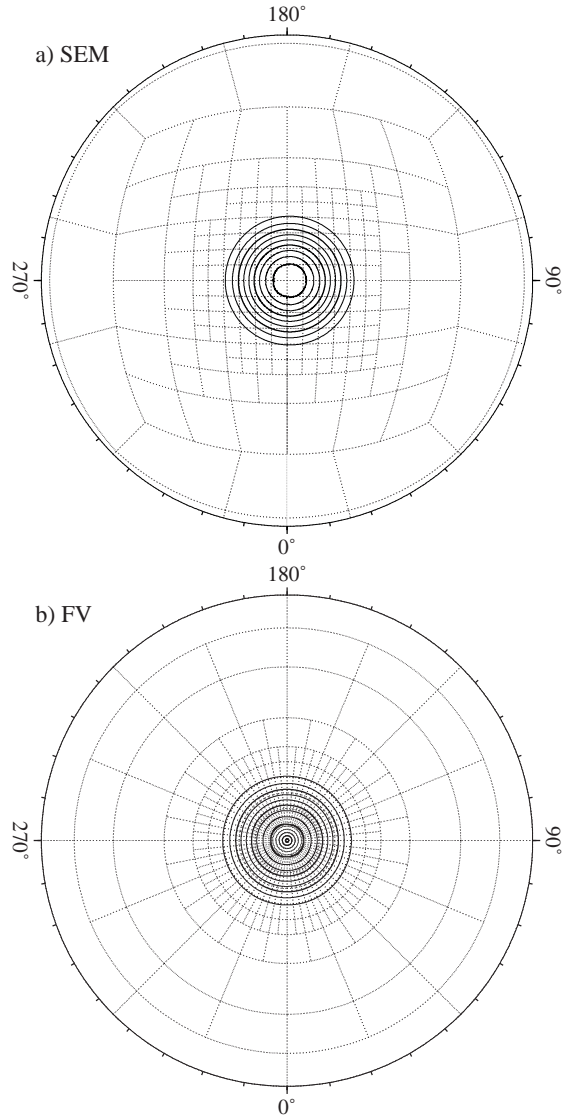


FIG. 5: North-polar stereographic projection of the cosine bell (test case 1) with rotation angle $\alpha = 90^\circ$ and three refinement levels at day 3 for (a) SEM and (b) FV. The finest grid spacing is $0.625^\circ \times 0.625^\circ$, the adapted spectral elements (SEM) and blocks (FV) are dotted. The contour interval is 100 m, the zero contour is omitted.

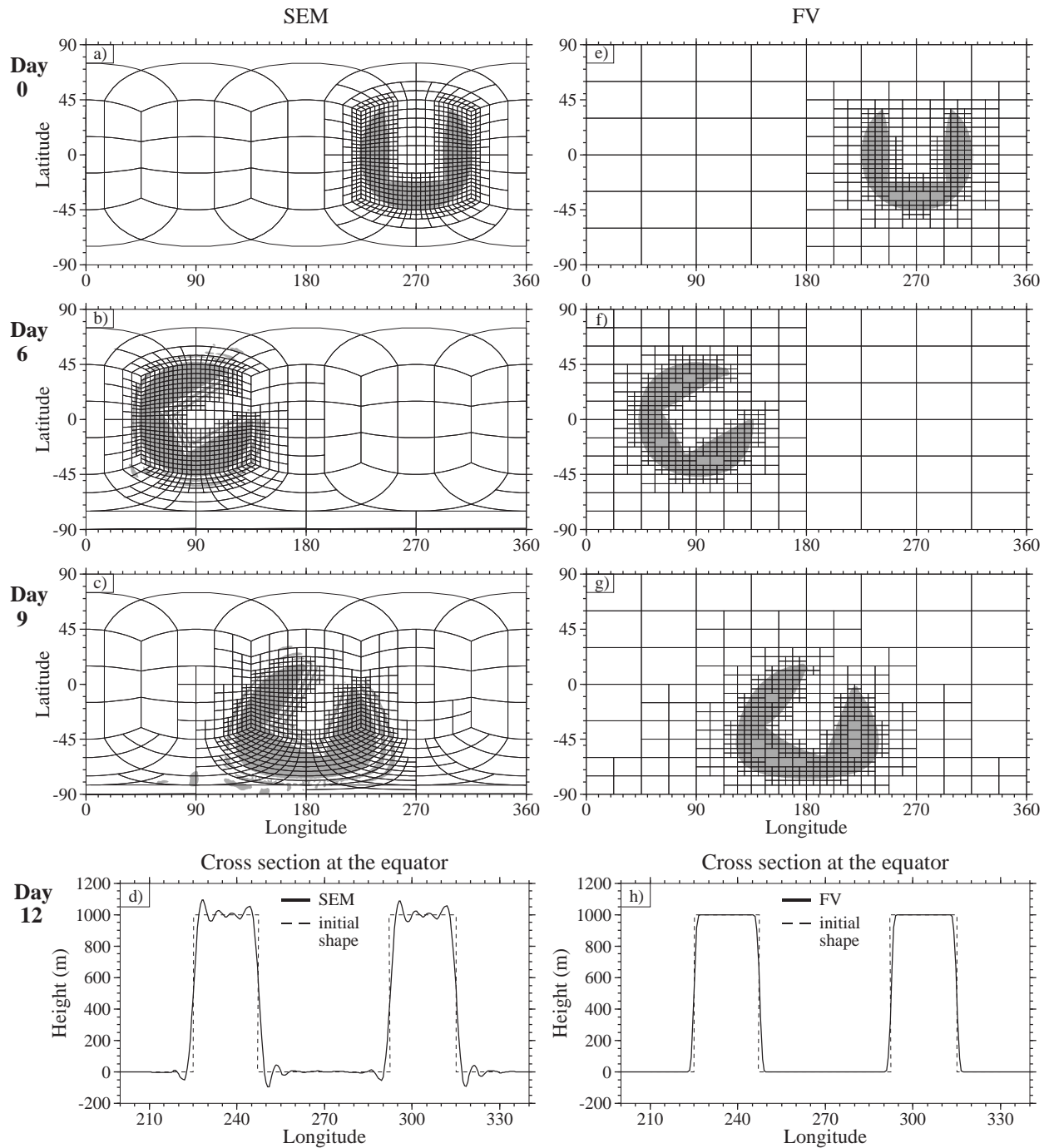


FIG. 6: Advection of a slotted cylinder with rotation angle $\alpha = 30^\circ$ and three refinement levels ($0.625^\circ \times 0.625^\circ$) in the models SEM (left column) and FV (right column). The height field with $h \geq 5$ m is shaded in gray. (a, e) Initial height field ($h = 1000$ m), (b, f) height field at day 6 (half a revolution), and (c, g) day 9. (d, h) Cross section of h along the equator at day 12 (full revolution). The adapted spectral elements (SEM) and blocks (FV) are overlaid.

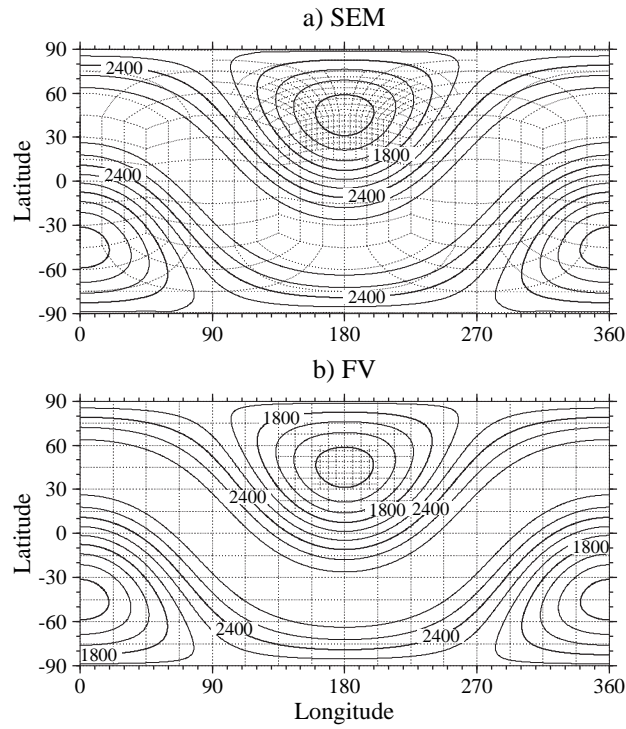


FIG. 7: Geopotential height field for test case 2 with $\alpha = 45^\circ$ at day 14 as simulated with the models (a) SEM and (b) FV. The statically adapted blocks with 2 refinement levels are overlaid (dotted contour). The refined patch is centered at $(180^\circ\text{E}, 45^\circ\text{N})$, the finest grid spacing is $0.625^\circ \times 0.625^\circ$. The contour interval is 200 m.

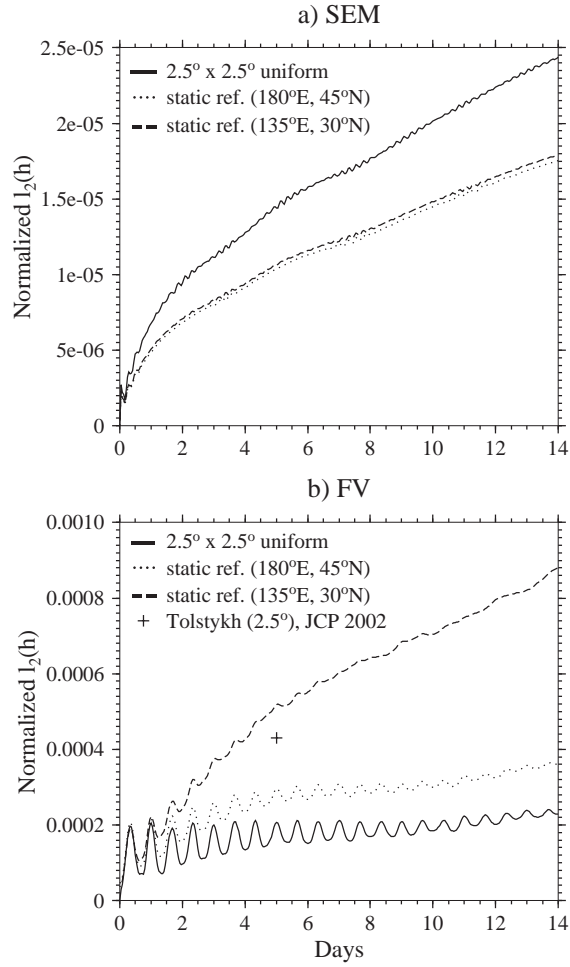


FIG. 8: Time traces of the normalized l_2 geopotential height error norms for the steady state geostrophic flow (test case 2) with rotation angle $\alpha = 45^\circ$. Two simulations with static refinement regions centered at $(180^\circ\text{E}, 45^\circ\text{N})$ and $(135^\circ\text{E}, 30^\circ\text{N})$ are compared to a uniform $2.5^\circ \times 2.5^\circ$ resolution run. The adaptive (a) SEM and (b) FV model runs start with a $2.5^\circ \times 2.5^\circ$ base grid with two refinement level (finest grid resolution is $0.625^\circ \times 0.625^\circ$.)

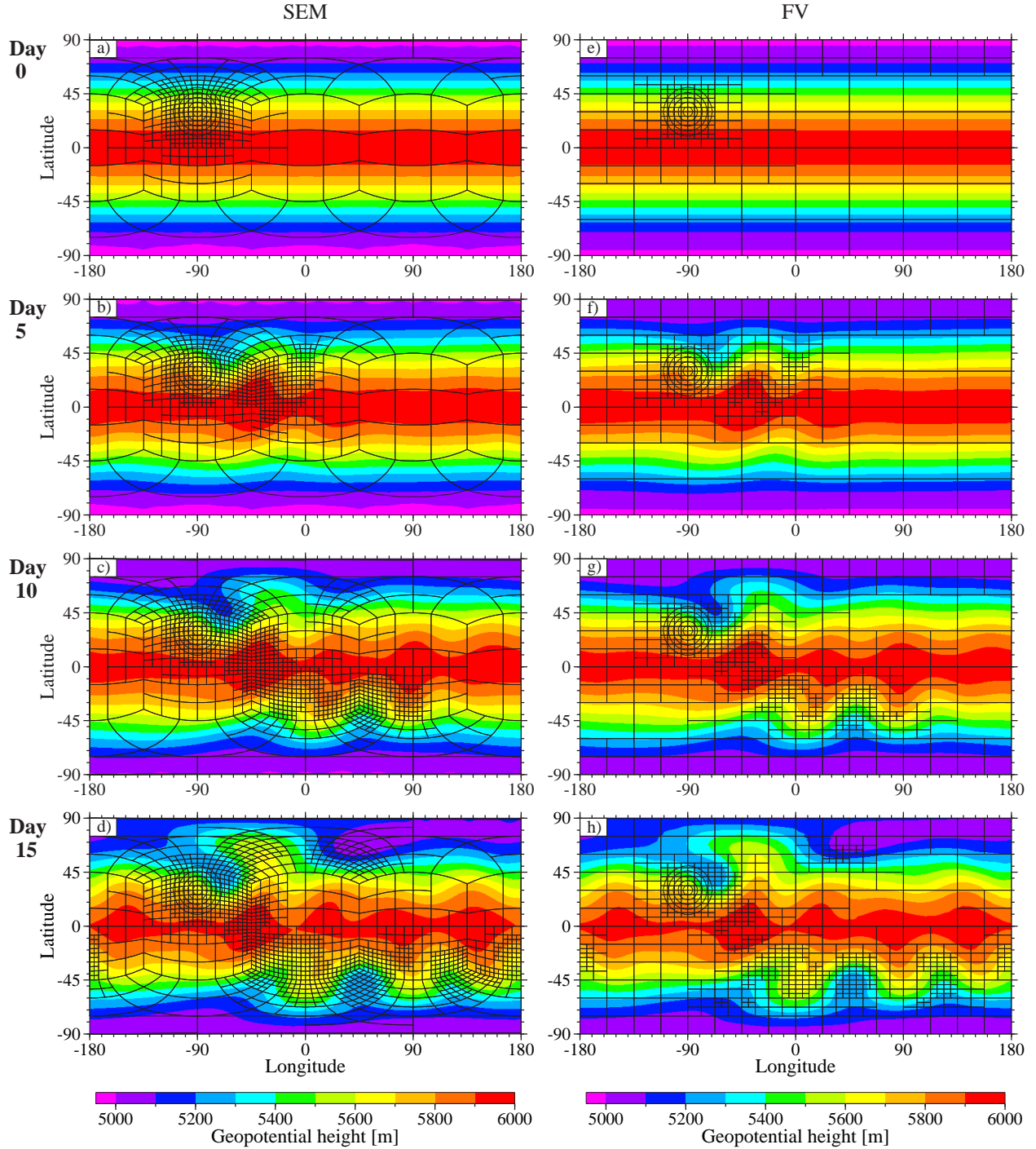


FIG. 9: Snapshots of the geopotential height field (test case 5, flow over a mountain) with three refinement levels at day 0, 5, 10 and 15. The finest grid spacing is $0.625^\circ \times 0.625^\circ$, the adapted spectral elements (SEM) and blocks (FV) are overlaid. Left column (a-d) shows the SEM model, right column (e-h) depicts the FV model. The refinement criterion is $|\zeta| \geq 2 \times 10^{-5} \text{ s}^{-1}$. The contour interval is 100 m.

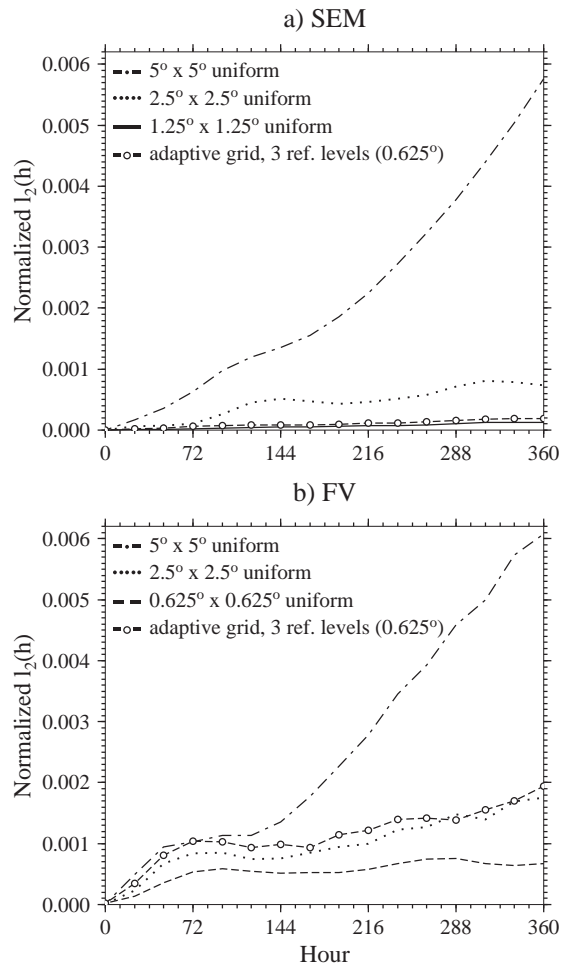


FIG. 10: Time traces of the normalized l_2 geopotential height error norms for the flow over a mountain (test case 5). The adaptive simulations with three refinement levels ($0.625^\circ \times 0.625^\circ$ at the finest level) and several uniform-resolution runs are compared to a T426 spectral transform reference solution.

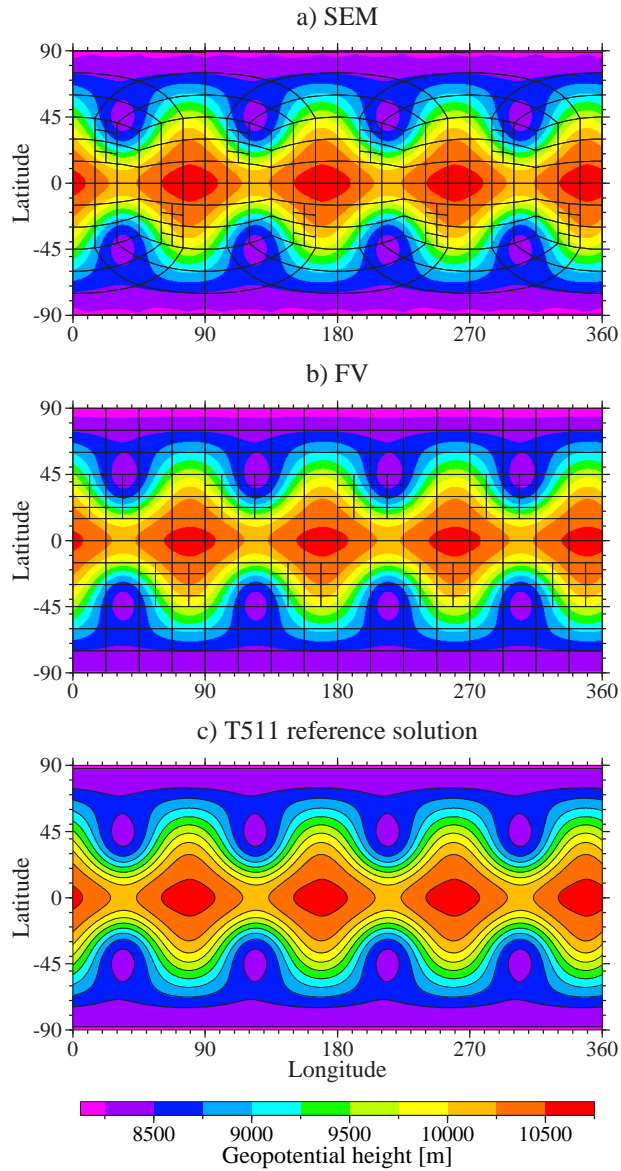


FIG. 11: Snapshots of the geopotential height field of the Rossby-Haurwitz wave (test case 6) at day 7 for (a) SEM, (b) FV and (c) the T511 spectral model (reference solution, NCAR model). SEM and FV utilize an adaptive grid with one level of static adaptations. The base resolution is $2.5^\circ \times 2.5^\circ$ and $1.25^\circ \times 1.25^\circ$ within the refined region. The adapted elements (SEM) and blocks (FV) are overlaid. The contour interval is 250 m.

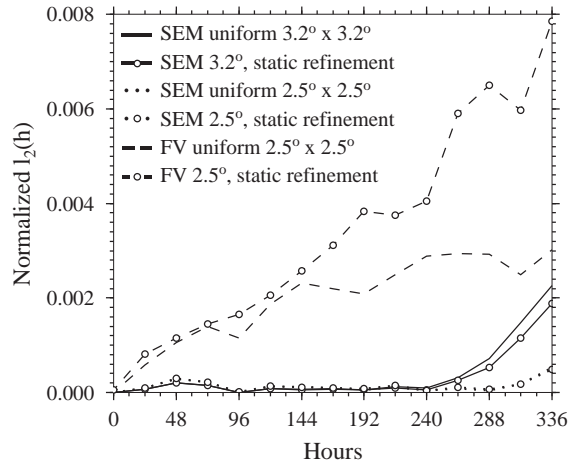


FIG. 12: Time traces of the normalized l_2 geopotential height error norms for the Rossby-Haurwitz wave (test case 6). The statically adaptive simulations with one refinement levels ($1.25^\circ \times 1.25^\circ$ at the finest level) and several SEM and FV uniform-resolution runs are compared to a T511 spectral transform reference solution. The uniform and adaptive SEM $2.5^\circ \times 2.5^\circ$ errors overlay each other.

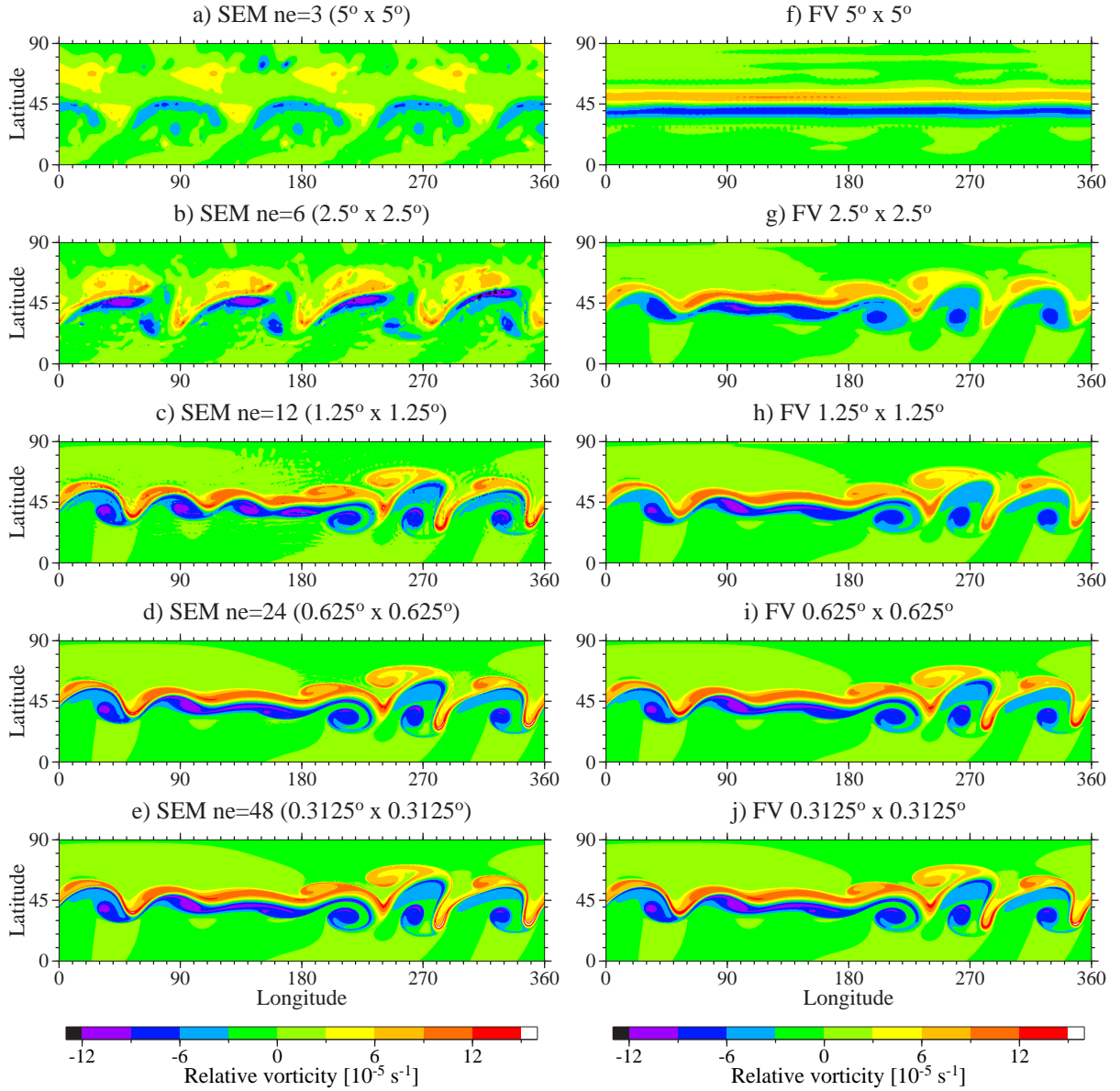


FIG. 13: Barotropic wave at day 6 in the models SEM (left column) and FV (right column) with uniform (non-adapted) grids at increasing resolutions as indicated above. The relative vorticity field ζ in the Northern Hemisphere is shown.

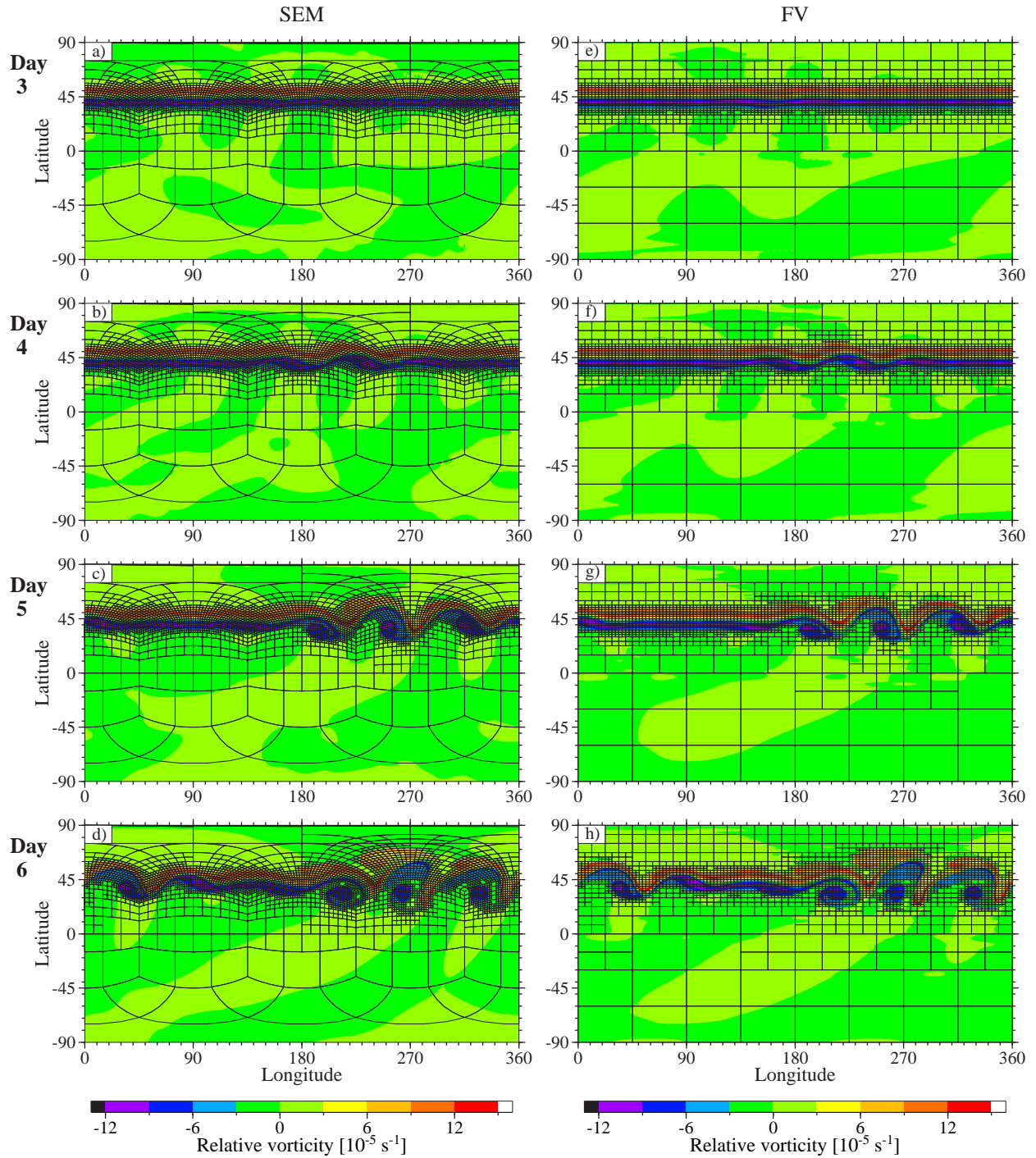


FIG. 14: Evolution of a growing barotropic wave in SEM (left column) and FV (right column) with four refinement levels (finest resolution is $0.3125^\circ \times 0.3125^\circ$). Snapshots of the relative vorticity field ζ at (a, e) day 3, (b, f) day 4, (c, g) day 5, and (d, h) day 6. The refinement criterion is $|\zeta| \geq 3 \times 10^{-5} \text{ s}^{-1}$, the adapted spectral elements (SEM) and blocks (FV) are overlaid.

TABLE 1: Overview of the resolutions in SEM. In each element, there are additional 6×6 GL points and 8×8 GLL points. ne is the number of spectral elements along one edge of one face of the cube.

SEM resolution ne	No. of elements per cubed face	Total no. of elements	Approximate resolution
3	3×3	54	$5^\circ \times 5^\circ$
4	4×4	96	$3.2^\circ \times 3.2^\circ$
6	6×6	216	$2.5^\circ \times 2.5^\circ$
12	12×12	864	$1.25^\circ \times 1.25^\circ$
24	24×24	3456	$0.625^\circ \times 0.625^\circ$
48	48×48	13824	$0.3125^\circ \times 0.3125^\circ$

TABLE 2: Statistics for the adaptive SEM and FV simulations. The test case numbers refer to the Williamson et al. (1992) test suite, the abbreviations 'cyl.' and 'wave' describe the slotted cylinder and barotropic wave test.

Test case	α	Base resolution	No. of ref. level	AMR	SEM		FV	
					Δt (s)	No. of elements	Δt (s)	No. of blocks
1	45°	5° × 5°	3	dynamic	10	231 (day 9)	adaptive	201 (day 9)
1	90°	5° × 5°	3	dynamic	10	237 (day 3)	adaptive	480 (day 3)
cyl.	30°	5° × 5°	3	dynamic	10	834 (day 12)	adaptive	507 (day 12)
2	45°	2.5° × 2.5°	2	static	10	462	200	288
5		5° × 5°	3	dynamic	20	1320 (day 15)	138	744 (day 15)
6		2.5° × 2.5°	1	static	15	264	225	288
6		3.2° × 3.2°	1	static	15	144	–	–
wave		5° × 5°	4	dynamic	3	3237 (day 6)	50	2550 (day 6)

TABLE 3: Normalized height error norms and characteristics for the advection of a cosine bell (test case 1) after one revolution (12 days) at different refinement levels and rotation angle $\alpha = 0^\circ$ for the models SEM and FV. All runs were started with the base resolution $5^\circ \times 5^\circ$. The third column indicates the resolution of the grid within the refined area.

Model	No. of ref. levels	Resolution $\Delta\lambda, \Delta\phi$	Day 12			$h(m)$ max / min
			$l_1(h)$	$l_2(h)$	$l_\infty(h)$	
SEM	1	2.5°	0.0503	0.0269	0.0195	991.6 / -15.1
SEM	2	1.25°	0.0085	0.0056	0.0057	997.5 / -4.2
SEM	3	0.625°	0.0019	0.0014	0.0019	999.1 / -1.1
SEM	4	0.3125°	0.0008	0.0006	0.0015	999.7 / -0.9
FV	1	2.5°	0.0341	0.0301	0.0317	949.1 / 0
FV	2	1.25°	0.0097	0.0103	0.0150	984.2 / 0
FV	3	0.625°	0.0016	0.0021	0.0044	995.0 / 0
FV	4	0.3125°	0.0003	0.0005	0.0014	998.4 / 0

TABLE 4: Run time statistics of the cosine bell advection test (test 1) for adaptive runs with 3 refinement levels and uniform resolution runs ($0.625^\circ \times 0.625^\circ$) with rotation angles $\alpha = 0^\circ$ and $\alpha = 45^\circ$. The number of time steps complete a full revolution (12 days). The approximate length of the time steps in the FV tests indicates that the time step is adaptive and therefore sometimes shorter than the most dominant value listed below. The wall clock time is the time needed for a 12-day simulation on one 1.9GHz IBM POWER5+ processor.

Model	α	Resolution $\Delta\lambda, \Delta\phi$	No. of ref. level	Day 12		Max. no. of blocks	Δt (s)	No. of time steps	Wall clock time (s)
				$l_2(h)$	$l_\infty(h)$				
SEM	45°	0.625°	0	0.0013	0.0014	3456	10	103680	7477
SEM	45°	5°	3	0.0013	0.0014	448	10	103680	644
FV	45°	0.625°	0	0.0080	0.0188	3072	13.12 (fixed)	79044	8119
FV	45°	5°	3	0.0082	0.0159	210	$\approx 206 - 809$	3714	66
FV	45°	5°	3	0.0080	0.0172	210	200 (fixed)	5184	90
FV	0°	0.625°	0	0.0020	0.0044	3072	≈ 1710	612	76
FV	0°	5°	3	0.0021	0.0044	204	≈ 1710	612	12

No. of processors	Breakdown of total AMR time in %			Wall clock time (s)		Ratio
	flops	comm.	overhead	AMR	FIXED	FIXED/AMR
8	78	8	14	3402	13116	3.9
16	61	9	30	2147	6172	2.9
24	48	8	44	1837	3972	2.2

TABLE 5: Wall clock execution times for 15-day SEM simulations for test case 5, flow over an idealized mountain, with 26 vertically stacked shallow water levels on a 1.9 GHz IBM POWER5+ system with 8, 16 and 24 processors. FIXED corresponds to a uniform 0.625° resolution grid, and AMR to a 5° base resolution with 3 refinement levels. The percentages indicate the time spent on the shallow water model (flops), the boundary data exchange (comm.) and the management of the AMR grid (overhead).